Energetic Phenomena on the Sun

Nat Gopalswamy

NASA Goddard Space Flight Center, Greenbelt, MD 20771, USA

Abstract. Solar flares, coronal mass ejections (CMEs), solar energetic particles (SEPs), and fast solar wind represent the energetic phenomena on the Sun. Flares and CMEs originate from closed magnetic field structures on the Sun typically found in active regions and quiescent filament regions. On the other hand, fast solar wind originates from open field regions on the Sun, identified as coronal holes. Energetic particles are associated with flares, CMEs, and fast solar wind, but the ones associated with CMEs are the most intense. The energetic phenomena have important consequences in the heliosphere and contribute significantly to adverse space weather. This paper provides an over view of the energetic phenomena on the Sun including their origin interplanetary propagation and space weather consequences.

Keywords: Flares; Coronal mass ejections; Solar energetic particles; Solar Wind; Space weather
PACS: 96.60.qe, 96.60.ph, 96.60.Vg

1. INTRODUCTION

Energetic phenomena refer to sudden increases in the energy output of the Sun in the form of electromagnetic radiation or mass emission. Transient increase in electromagnetic radiation is known as a solar flare. There are two types of energetic mass emissions: coronal mass ejections (CMEs), and solar energetic particles (SEPs). Normal solar wind blowing past Earth has a speed of ~400 km/s, but occasionally the speed increases to ~700 km/s. This energetic solar wind is also known as fast solar wind or high-speed stream. The energetic phenomena originate from specific magnetic structures on the Sun. CMEs and flares originate in closed magnetic structures, while the fast wind originates from open structures. Closed-field regions contain positive and negative polarities, whereas the open field regions are approximately unipolar. The field lines from the open regions (coronal holes) connect to infinity. When the high-speed streams compress the slower wind ahead, interaction regions are produced. When these interaction regions are recurrent, they are known as corotating interaction regions (CIRs). Sometimes energetic particles are also accelerated in the interaction regions.

Although the energetic phenomena are linked to solar magnetic fields, we do not fully understand how the energy is released. Various physical processes are involved: plasma instabilities, magnetic field reconnection, wave-particle interaction, bulk-plasma energization, shock formation, particle acceleration, and so on. Thus studying the energetic solar phenomena helps us understand many physical processes over very large scales compared to terrestrial systems. In addition to the physics, there are also practical implications. While the steady energy output of the Sun supports life on Earth, the energetic phenomena can be hazardous to human activities in space and even to life. For example the near-Earth space can be filled with particle radiation (SEPs) for several days during a CME event. SEPs can destroy electronics on spacecraft and harmful to

CP919, *Kodai School on Solar Physics,* edited by S. S. Hasan and D. Banerjee
2007 American Institute of Physics 978-0-7354-0429-8/07/$23.00

astronauts. Satellite-based communications can be severely hampered by adverse space weather. Solar energetic phenomena can affect almost the entire heliospace, the physical space controlled by the Sun up to the local interstellar medium. CMEs propagating into the heliosphere have also the beneficial effect of deflecting the galactic cosmic rays that enter the heliosphere. CMEs impacting Earth's magnetosphere can cause major geomagnetic storms that lead to a number of effects in the ionosphere, atmosphere, and on the ground (disruption of power lines, railroads, and pipelines). CIRs impacting Earth can also lead to geomagnetic storms, generally of lower intensity, but result in high levels of harmful high-energy electrons in the magnetosphere.

2. SOLAR MAGNETISM, ACTIVE REGIONS, AND CORONAL HOLES

The photospheric magnetic field is organized in patches of strong field embedded in an overall weak field (see Fig. 1). During solar maxima, the large-scale field is in active regions (ARs), which typically consist of two spots of opposite polarity surrounded by faculae. ARs occur in two parallel bands one on either side of the equator (known as active region belts). The leading polarity in the active region fields is opposite in northern and southern hemispheres and switches every 11 years (the Hale & Nicholson [1] law). Magnetic flux emergence is the key to the connection between magnetic field generation in the Sun, and the appearance of active regions on the surface and above. An east-west oriented flux tube embedded in the convection zone is lifted up due to the buoyancy force into low density regions. Penetration of this field through the solar surface produces the observed bipolar structure in active regions. How the east-west flux rope is produced inside the Sun is actively debated by the dynamo theorists. The AR fields decay in a few months as small-scale magnetic elements. ARs tend to originate in the sites of existing or previous ARs. AR emergence results in the butterfly pattern: sunspots appear at mid latitudes during solar minimum and progressively emerge closer to the equator as the solar cycle proceeds.

ARs have been classified in several ways, but the Mt. Wilson classification introduced by Hale et al. [2] is the simplest and is based on the polarity of the sunspots: 1) Alpha: a single dominant spot, often linked with a plage of opposite magnetic polarity, 2) Beta: A pair of dominant spots of opposite polarity (bipolar), 3) Gamma: complex groups of spots with irregular distribution of polarities, 4) Beta-gamma: bipolar groups which have more than one clear north-south polarity inversion line, and 5) Delta: umbrae of opposite polarity together in a single penumbra. The smaller magnetic elements in Fig. 1 occur at the boundaries of super granulation on the Sun and is present more or less uniformly throughout the solar surface.

Figure 2 shows the Sun during October 17-18, 1999 observed at four different wavelengths, corresponding to four different heights in the solar atmosphere: a longitudinal magnetogram from the Solar and Heliospheric Observatory (SOHO) mission's Michelson Doppler Imager (MDI), an H-alpha picture from the Big Bear Solar Observatory, an extreme ultraviolet (EUV) image at 195 ï£¡from SOHO, and a soft X-ray image obtained by the Yohkoh mission. The AR complex appears brightest in all images. The active region loops are hotter and denser and hence have bright coronal emission. The elongated

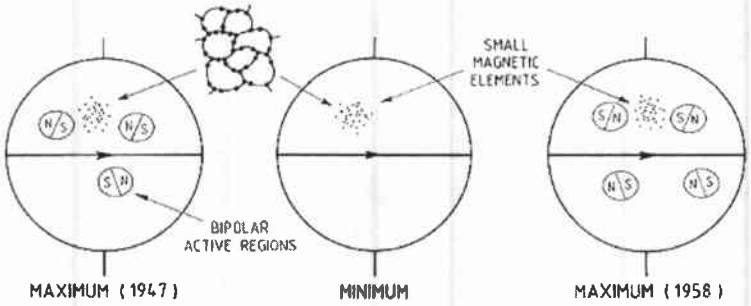

FIGURE 1. Large (active regions) and small-scale magnetic elements observed on the Sun. The large-scale structures change the polarity every 11 years (compare 1958 solar maximum phase with the preceding one in 1947). During solar minima, there are not many active regions. The small-scale fields are organized in networks. N and S denote the north and south polarities within active regions. Each polarity will have one or more sunspots, sometimes no spot. The slanted line between S and N represents the polarity inversion line (from Hoyng [3].

dark features are the filaments, which delineate opposite polarity patches both in the AR and in the quiet regions. Filaments are observed in absorption because they are cool (~ 8000 K), but they are seen in emission when seen above the limb and they are known as filaments. A transequatorial interconnecting loop (TIL) structure can be seen in the X-ray and EUV images, connecting ARs in the northern and southern hemispheres. One can also see coronal holes, which appear as dark patches in the X-ray and EUV images. The magnetic field inside the largest coronal hole in the northwest quadrant is enhanced and unipolar (positive).

3. HIGH-SPEED SOLAR WIND

Fast solar wind was detected by Mariner 2 spacecraft in 1962 and was also found to recur after 27 days, the rotational period of the low-latitude Sun. The discovery of coronal holes in 1973 in X-rays by the Skylab mission revealed that the fast wind originates from coronal holes. Coronal holes appear dark in X-rays because they are cooler and less dense compared to the surrounding quiet corona. Figure 3 shows a complex coronal hole observed on 2003 July 13 by SOHO in the 284 ï£¡line. The compact bright regions are the closed field regions as in Fig. 2. The diffuse bright regions represent the quiet corona. The dark region (with three arms) is the coronal hole. Fast wind blows radially away from coronal holes, so when Earth faces a hole, it gets immersed in the fast wind. Coronal holes need to be present within ~30° latitudes to be intercepted by Earth. A 600 km/s stream reaches Earth in ~3 days. The Sun rotates at the rate of ~13°.5 per day, so by the time the solar wind reaches Earth, the wind source rotates by 40° to the west. When the coronal hole is extended in the east-west direction, prolonged periods of high-speed wind is likely to hit Earth. The variability in the solar wind speed shown in Fig. 3 reflects the inhomogeneous nature of the extended coronal hole. Equatorial coronal holes

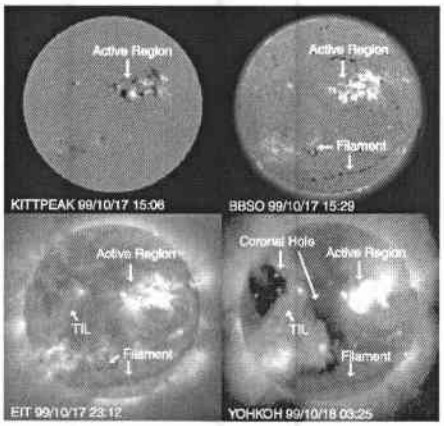

FIGURE 2. Examples of closed (active regions, filaments, TIL) and open (coronal holes) magnetic filed regions on the Sun on the Sun as revealed by a magnetogram obtained by the national Solar Observatory in Kitt Peak (top-left), A H-alpha picture from the Big Bear Solar Observatory (top-right), an EUV image (false-color) obtained by SOHO showing the coronal counterpart of active regions (bottom-left), and an X-ray image of the corona obtained by the Yohkoh satellite (bottom-right). TIL: transequatorial interconnecting structures.

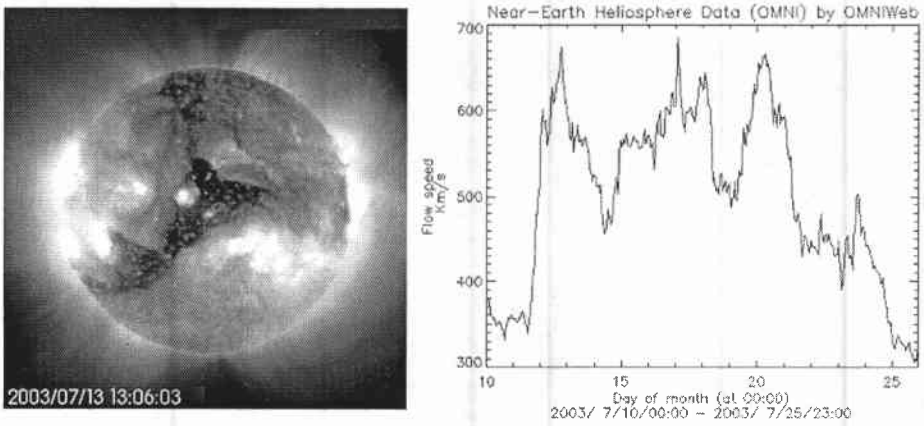

FIGURE 3. An image of the solar corona taken in the 284 ï£¡EUV line by SOHO (left) and the solar wind speed measured at 1 AU for a 1 6-day period from July 10 to 26, 2003 (right).

are generally transient (they typically last for a few solar rotations), whereas the polar coronal holes are more or less permanent during solar minima. High-speed wind from polar holes has been consistently observed by the Ulysses spacecraft at a distance of several AU (AU is the astronomical unit, measured as the average Sun-Earth distance). High-speed wind from polar coronal holes are readily measured from interplanetary scintillation (IPS) observations (See Manoharan [4], this volume).

The dark region on the Sun is the coronal hole, extending from the west limb of the Sun to slightly east of the disk center. It also has extensions to the north and southeast. The coronal holes are not 'holes' at all wavelengths: In microwaves they appear bright over a narrow frequency range (15-40 GHz). At frequencies higher than ~40 GHz, coronal holes are indistinguishable from the quiet Sun; at frequencies lower that ~15 GHz, coronal holes are dimmer than the quiet region. The frequency range of microwave enhancement corresponds to the plasma frequency of the upper chromosphere and may be linked to the solar wind origin (Gopalswamy et al. [5]), as indicated by Doppler shift in Ne VIII spectral lines (Hassler et al. [6]). Recent observations confirm that the solar wind originates in the height range of 5000-20000 km above the photosphere (Tu et al. [7]).

Coronal holes are also responsible for moderate geomagnetic storms when the high-speed wind impacts on Earth's magnetosphere. In fact, even before the discovery of coronal holes and solar wind, recurrent geomagnetic variations were attributed to Bartel's M- regions (see Zirker [8]). The storm happens when the compressed region between high and slow winds sweeps past Earth. It is now known that the magnetic field in the coronal holes is enhanced but mostly unipolar.

4. SOLAR FLARES

A solar flare can be defined as a sudden and rapid release of energy from a localized region on the Sun mainly in the form of electromagnetic radiation over the entire spectrum. R. C. Carrington and R. Hodgson observed a flare for the first time on September 1, 1859. Solar flares directly impact Earth's atmosphere by enhancing the ionization in the ionosphere, thus affecting communications which depend on stable ionospheric conditions. Occasionally microwave emission from flares can jam GPS receivers temporarily rendering them useless. Temperature in the flaring region can reach more than 10 MK, providing opportunity to study large volumes of high-temperature plasmas that are not easy to create in the laboratory.

Flares are observed at almost all wavelengths, from gamma rays to kilometric radio waves. The emission produced at different wavelengths may be due to different mechanisms. Some are thermal emission resulting from the high temperature plasmas produced during flares and others are nonthermal emission resulting from accelerated electrons. Extensive literature exists on flares: detailed discussion can be found in Svestka [9] and Zirin [10].

Systematic flare observations were made in the Hydrogen Balmer line (6563 ï£¡ commonly known as H-alpha line. While the white-light flare is an enhancement in continuum radiation, the H-alpha flare is a temporary emission within the dark Fraunhofer line. The current understanding of the optical emissions is that energetic electrons accelerated in the corona flow down and heat the chromosphere producing the H-alpha emission. H-alpha emission is normally seen as two ribbons evolving in time (see Fig. 4). Dark loops straddle the two ribbons as the flare decays forming an arcade with its axis roughly parallel to the ribbons. These observations provide a general geometry of the flares involving closed magnetic structures with their feet rooted on the opposite polarity fields in active regions. Filaments are also often seen ejected from above the

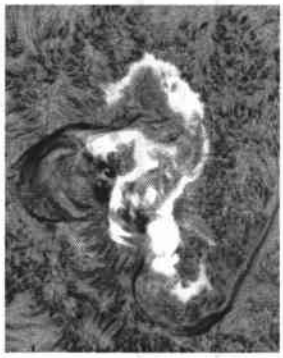

FIGURE 4. H-alpha picture of the famous two-ribbon flare of August 7, 1972. The two white ribbon-like structures (roughly parallel to each other) mark H-alpha emission from the chromosphere The elongated dark linear features are the filaments (cool material at a temperature of ~8000 K), which mark the magnetic neutral line between the ribbons. Dark loops straddling the ribbons are known as post-flare loops or simply flare loops. They appear bright in X-ray and EUV wavelengths. A similar filament located between the flare ribbons had erupted as part of the flare. The size of the picture is 120 arcsec × 150 arcsec. Courtesy: Big Bear Solar Observatory

TABLE 1. Optical and radio classification of flares.

Flare Area msh (Sq. degree)	Faint	Normal	Brilliant	Radio Flux (SFU)
<100 (<2.06)	Sf	Sn	Sb	<5
100–250 (2.06–5.15)	1f	1n	1b	30–1300
250–600 (5.15–12.4)	2f	2n	2b	1300–23000
600–1200 (12.4–24.7)	3f	3n	3b	23000–30000
>1200 (>24.7)	4f	4n	4b	>30000

neutral line, and if this happens, the flare is known as an eruptive flare, as opposed to confined flare that has no mass motion.

The area of the H-alpha brightening decides the optical flare size: for large flares, the area can exceed 10^9 km^2, while it can be smaller than 3×10^8 km^2 for tiny flares. H-alpha flare area (measured as the number of square degrees; 1 heliographic degree = 12500 km) has been used as the basis for defining optical flare importance. The size is also given by the millionths of solar hemisphere (msh): $\sim3\times10^6$ km^2. A scale of 0 - 4 is used to denote the H-alpha flare importance (i.e., S, 1, 2, 3, 4) with additional suffix for brightness (F-faint, N-normal, B- brilliant). The lowest importance is denoted by S (for subflare). According to this scale, 4B denotes the highest importance and SF the lowest.

In addition to the optical observations, the radio window provides another technique to observe flares from millimeter to meter waves. The radio emission is produced by nonthermal electrons with energies ranging from a few keV to > 1 MeV. A variety of mechanisms operate at radio wavelengths from free-free emission and gyrosynchrotron at shorter wavelengths to coherent plasma emission at metric and longer wavelengths. Radio observations provide unique information on the magnetic field in the flare loops

TABLE 2. Soft X-ray Flare Classification.

Flare Importance	Peak Flux (W m^{-2})
A	$< 10^{-7}$
B	10^{-7} to 10^{-6}
C	10^{-6} to 10^{-5}
M	10^{-5} to 10^{-4}
X	$> 10^{-4}$

and the surrounding plasma through which energetic electrons propagate. Microwave emission at 5 GHz is typically used to estimate the flare sizes in terms of solar flux units (sfu). The unit of radio flux is 1 sfu = 10^{-22} Wm^{-2}. The radio flux has an approximate correspondence to the flare importance: I = log S - 0.5, where S is the radio flux and I the H-alpha flare importance. Table 1 shows the flare classification based on H-alpha and microwaves.

Earth's atmosphere blocks most of the other wavelengths, so we have to go to space to detect flares in UV, X-rays, and gamma rays. At wavelengths longer than decametric, we need to go above Earth's ionosphere because the plasma frequency of the ionosphere is around 15 MHz, so radiation at lower frequencies cannot penetrate the ionosphere.

Soft X-ray Flares: With the advent of space based observations in the 1960s, flares have been extensively observed in soft X-rays (in the 1-10 ï£¡ wavelength range). Two soft X-ray channels (1-8 ï£¡and 0.8 - 4 ï£¡from GOES) have provided extensive data on solar flares for decades. The soft X-ray emission is mostly thermal emission from the flaring corona with a temperature of a few MK to more than 10 MK. Since the peak wavelength (λmax) of thermal radiation is determined by the temperature (T) according to λmaxT = 0.29, we see that a 10 MK plasma mainly emits at λmax = 2.9×10^{-8} cm or 2.8 ï£¡ Thus the bulk of the radiation in flare plasma occurs in soft X-rays. The global photon output in the 1-8 ï£¡ channel (no spatial resolution) measured as W m^{-2} is currently used to denote the soft X-ray flare size. Originally the letters C, M, and X were used to denote flares with peak intensity within an order of magnitude from 10^{-6}, 10^{-5}, and 10^{-4} W m^{-2}, respectively. Letters A ($< 10^{-7}$ W m^{-2}) and B (10^{-7} to 10^{-6} W m^{-2}) were added later on to denote weaker flares (see Table 2). For example, an M5.3 flare has a peak flux of 5.3×10^{-5} W m^{-2}. Flares larger than X10 are simply denoted by stating the multiplier, e.g. X28 for a flare with peak intensity 2.8×10^{-2} W m^{-2}.

Figure 5 shows two flares with extremely different sizes. One is an X-class flare and the other is an A-class flare observed during solar minimum. The background levels are also very different because of the phase of the solar cycle. In soft X-ray images, weak flares can be observed more clearly. In fact there was a weak arcade formed just before 18:00 UT on 1997 October 6, which lasted for a few hours. Soft X-ray images from Yohkoh revealed the broad range over which the flare arcades were seen. Figure 6 shows a soft X-ray flare loop obtained with an aluminum (Al 12) filter. The bright loop is due to a flare. Microwave emission was also observed from the flare loop, as shown by the contour maps at two frequencies. The 5 GHz emission comes from the loop top, while the 17 GHz emission comes from the loop legs. The frequency of emission is decided by the local magnetic field in the loop. Higher frequency emission comes from lower

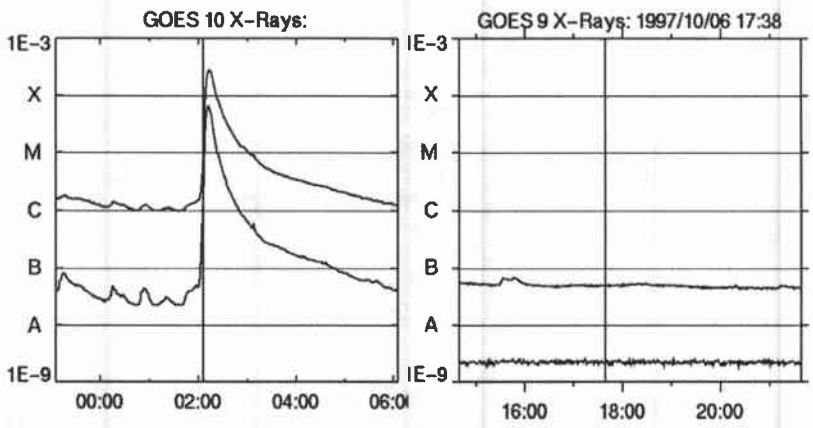

FIGURE 5. Examples of GOES soft X-ray flares of X (left) and A (right) classes. The soft X-ray levels are marked on the Y-axis according to the classification in Table 2. The vertical lines indicate the times of large scale mass motion, which will be discussed in the next section.

in the loop, where the magnetic field is also higher. This figure illustrates both thermal (soft X-rays) and nonthermal (microwave) emissions from the flare loop.

Hard X-ray Flares: When the X-ray photons have energy of a few keV, they are called soft X-rays. Photons in the energy range 10 - 300 keV are known as hard X-rays. Hard X-rays are emitted when the accelerated electrons from the corona collide with protons in the denser chromosphere via the well known process of bremsstrahlung. The photon energy roughly corresponds to the initial energy of the electrons, so it is possible to estimate the distribution of nonthermal electrons from the observed photon spectrum. Hard X-ray emission marks the "impulsive phase" of flares, when the hot thermal plasma emitting soft X-rays has not yet been produced in significant quantities by the thermalization of the accelerated electrons. In images, hard X-ray sources are located on either side of the neutral line, suggesting the loop structure along which the electrons flow down (see Fig. 7). Hard X-ray flares are classified (Dennis [11]) as thermal flares (smooth time profile of emission from compact single loop), impulsive (larger loops exhibiting spiky time profile), and gradual flares (very large loops lasting for hours).

EUV: The flare emission in extreme ultraviolet wavelengths originates from the chromosphere, transition region, and corona (temperature range: 10^4 -10^6 K). Both line emissions and continuum are observed in EUV. SOHO mission's Extreme-ultraviolet Imaging Telescope (EIT) has revolutionized the study of the Sun by capturing the dynamic behavior of the corona in EUV spectroheliograms: 171 ï£¡(FeI X/X), 195 ï£¡(Fe XII), 284 ï£¡(Fe XV), and 304 ï£¡ (He II). The coronal EUV spectroheliograms resemble soft X-ray images, especially the ones in 284 ï£¡

Gamma Rays: Both continuum and line emissions are observed in gamma rays. The line emission is from nuclear processes resulting from ion bombardment, while the continuum is due to bremsstrahlung from relativistic electrons from the same flare. Gamma ray line emissions provide important clues to accelerated ions during flares,

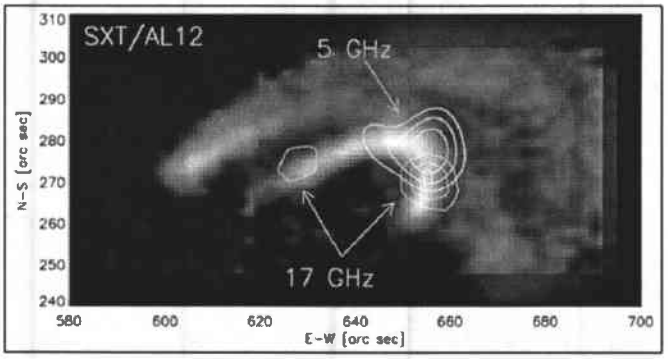

FIGURE 6. A soft X-ray flare loop with superposed microwave sources at 17 GHz and 5 GHz. At 17 GHz, the radio sources are seen at both legs of the loop, while it is only at the loop top at 5 GHz (from Lee et al. [12]). The radio emission is due to gyrosynchrotron emission from 100s of keV electrons. The emission occurs high harmonics (10-100) of the gyrofrequency (fc = 2.8B MHz where B is the magnetic field in the loop).

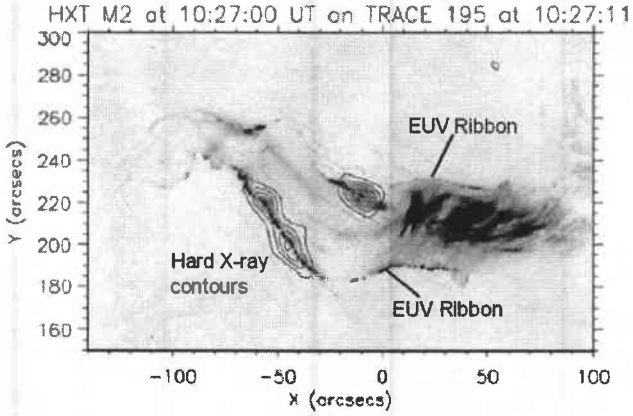

FIGURE 7. Hard X-ray contours from the Hard X-ray Telescope (HXT) on board Yohkoh superposed on flare ribbons observed by TRACE satellite in EUV (195 ï£¡. Note that hard X-ray emission is patchy compared to the extended ribbons observed in EUV. The flare ribbons are similar to the ones in H-alpha. The overlying arcade is also seen to the right. The two observations are only 11 s apart (adapted from Fletcher & Hudson [13]).

unlike in other wavelengths. Accelerated ions excite nuclei in the solar atmosphere whose deexcitation results in lines in the 1-8 MeV range. Two prominent lines occur at 4.43 MeV (due to deexcitation of carbon nuclei) and 6.14 MeV (due to deexcitation of oxygen nuclei). Radioactive nuclei also emit gamma rays and positrons. The positrons annihilate with electrons to produce the 0.511 MeV line. Pions produced during the nuclear processes decay into electrons, positrons, neutrinos and gamma rays. Neutrons produced as a result of ion impact can either be detected directly on Earth or indirectly

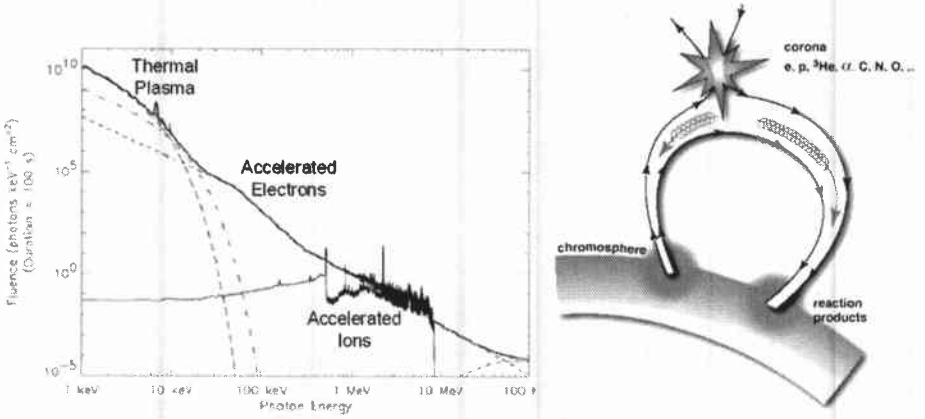

FIGURE 8. (left) A composite spectrum of X-rays and gamma rays during a large flare. The first two sections of the spectrum (below 10 MeV) are due to thermal emission. The next section up to a few hundred keV are due to nonthermal bremsstrahlung from energetic electrons. The section beyond ~300 MeV are due to relativistic electrons. The spiky features are nuclear line emissions. The first prominent peak is the positron annihilation line at 0.511 MeV. The most prominent line is the 2.223 MeV line. The 4.43 and 6.15 MeV lines are also seen. The rising continuum beyond 10 MeV (dashed line) is the pion continuum (courtesy: G. Holman). (right) A flare loop carrying energetic particles in helical paths flowing down from the corona and bombarding the chromosphere where they create the nuclear reaction products and nonthermal bremsstrahlung. The location where flare loop intersects the chromosphere is also the location of H-alpha ribbons and hard X-ray footpoints (from Share & Murphy [14]).

by neutron capture on hydrogen producing the characteristic 2.223 MeV line. Figure 8 shows a composite fluence spectrum of X-rays and gamma rays during a large solar flare and the particles accelerated in the corona flowing down along magnetic loops. The reaction products in the solar atmosphere are also shown schematically. The sources of radiation at various energy ranges are also indicated. Low-energy X-ray emission comes from the heated flare plasma. The continuum emission at energies > 10 MeV is due to energetic electrons. The superposed lines are all due to energetic ions impinging on the chromosphere.

From the flare observations we have discussed so far, it is clear that one or more loops are involved in the flare with energy released in the form of accelerated ions and electrons flow down to the lower atmosphere producing various kinds of emission. Nonthermal electrons produce X-rays, microwave, and gamma rays while ions produce gamma ray lines. Thus we can study the acceleration region and the solar atmosphere where they deposit energy from flare observations at various wavelengths. We have paid attention mainly to the particles flowing down. Particles accelerated in the corona can also propagate away from the Sun into the interplanetary medium, producing various types of radio bursts (see Kundu [15], Zheleznyakov [16]). Beams of nonthermal electrons propagating away from the Sun are unstable to high-frequency plasma waves known as Langmuir waves. The beam energy goes into plasma waves, which then get converted into electromagnetic waves observed as radio bursts. The movement of the electron beam through the corona is inferred from the drift of the radio emission from higher to lower frequen-

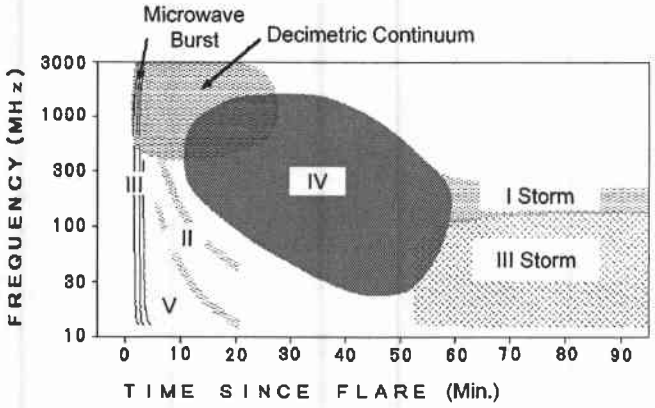

FIGURE 9. Time vs. Frequency plots of solar radio emission. Both continuum and bursts are observed. Type III bursts are due to electron beams. Type IV burst is a variant of type III burst propagating through curved field lines. Type IV emission is a continuum emission due to nonthermal electrons trapped in flare loops. Type II bursts are due to shock-accelerated electrons. Type I and type III continuum are not closely related to flares, but cab develop after big flares. (Adapted from Hiraiso/NiCT web site, Japan)

cies (the electron density in the corona decreases as one goes away from the Sun and the characteristic plasma waves have a frequency proportional to the square root of the electron density). The radio bursts are known as type III radio bursts for historical reasons. Figure 9 shows a schematic of various types of radio bursts observed during flares. Some are directly related to flares, others due to mass motions. Protons and heavier ions also propagate outwards as detected in the interplanetary medium as SEP events, which provide information on the source conditions such as temperature and density. Prominence eruptions and X-ray plasmoids are also ejected away from the Sun in association with flares, but these may not be caused by flares; instead flares seem to be the response to such eruptions.

5. CORONAL MASS EJECTIONS

Coronal mass ejections (CMEs) involve large chunks of the solar corona overlying closed magnetic regions blown off into the interplanetary medium carrying plasma and magnetic field with kinetic energies as high as 10^{26} J. The energy content of the active region magnetic fields is sufficient to power such violent events, but the exact mechanism is poorly understood. The mass involved in the ejection could easily exceed 10^{16} g with speeds occasionally exceeding 3000 km/s. Large-scale mass motions of this energy can easily drive fast-mode MHD shocks, which in turn accelerate SEPs. When CMEs are ejected in the direction of Earth, they can impinge on Earth's magnetosphere causing huge geomagnetic storms. Geomagnetic storms result in intense aurora and can significantly affect the ionospheric conditions.

Compared to flares, CME is a recently discovered phenomenon, first detected in

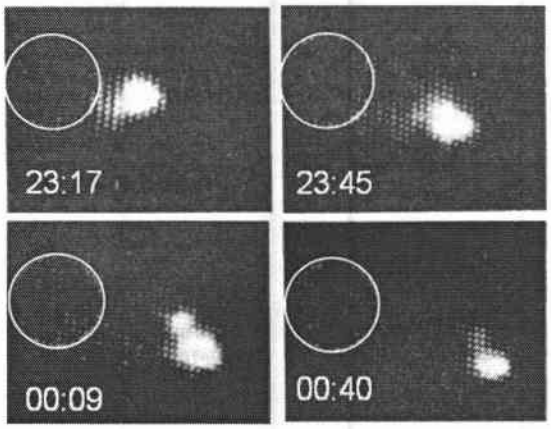

FIGURE 10. A moving type IV radio burst observed on 1969 March 1. The white circle is the optical disk of the Sun. Note that the burst has moved several solar radii in 83 minutes. The moving type IV radio bursts at metric wavelengths are produced by nonthermal electrons trapped in moving plasma structures (Riddle [20]). CMEs are now understood as large-scale magnetized plasma structures originating from closed magnetic field regions on the Sun: active regions, filament regions, active region complexes. Moving type IV bursts, eruptive prominences, and X-ray plasmoids are observed as substructures of CMEs.

the coronagraph images obtained on 1971 December 14 by NASA's OSO-7 spacecraft (Tousey [17]). However, mass ejections in the solar atmosphere were known decades before the white-light discovery: prominence eruptions [Secchi and de la Rue in the late 1800s (see, e.g., Tandberg-Hanssen [18])], slow-drifting radio bursts (Payne-Scott [19]), and moving type IV radio bursts (Boischot [21]). Rapid decay of transient coronal condensation (Hansen et al. [22]), coronal green line transients (DeMastus et al. [23]), helium abundance enhancements in the high speed plasmas behind interplanetary shocks (Hirshberg et al. [24]) are now recognized as different manifestations of CMEs. Figure 10 shows a moving type IV burst, indicative of the motion of a large-scale coronal plasma, imaged by the Culgoora radioheliograph in 1969 at 80 MHz (Riddle [20]). Note that the size of the radio burst is $\sim$1 $R_{\odot}$ (700,000 km) and can be tracked to a distance of several solar radii. A list of review articles covering the three decades of CME research can be found in Gopalswamy [25]. Recent collections of articles on CMEs can be found in two monographs: Kunow et al. [26] and Gopalswamy et al. [27].

5.1. Definition of a CME

Figure 11 shows a large-scale CME ejected from above the east limb of the Sun as observed by the Large Angle and Spectrometric Coronagraph (LASCO) on board SOHO (Brueckner et al. [28]). The coronagraph image at 16:50 UT on 2001 April 5 shows only some small changes in the corona due to streamer changes. The image at 17:26 UT shows a large-scale feature above the entire east limb with its leading edge at a distance

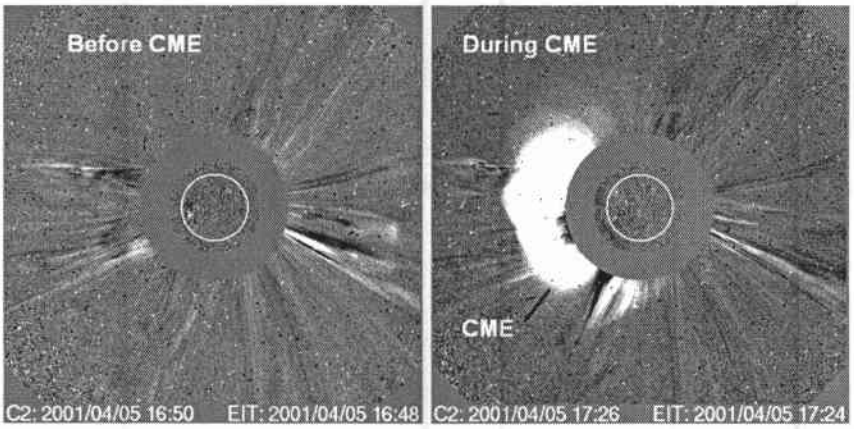

FIGURE 11. Two images of the corona obtained by the SOHO coronagraph. In the left image, the corona is quiet with small-scale changes in the streamers. In the right image, taken ~36 min later, a large-scale feature can be seen above the east limb of the Sun. The white circle denotes the optical Sun. The gray disk is the occulting disk to block the photospheric light so the faint coronal emission can be imaged. Note that the CME is much bigger than the optical Sun and gets even bigger as it expands and moves out. There are also disturbances at the outskirts of the CME.

of 4.8 $R_\odot$. The central part of the CME makes an angle of 58° to the solar north and this angle is known as the central position angle. The angular extent of the CME between the upper and lower edges is more than 90°. The CME moved out with a speed of ~1390 km/s. The CME erupted from a region close to the east limb of the Sun, as evident from the EUV image at 16:48 from SOHO/EIT superposed on the 16:50 LASCO image. The location of the eruption on the disk is referred to as the solar source of the CME. This location is usually the coordinates of the associated flare in H-alpha or the site of an eruptive prominence.

5.2. Morphological properties

CMEs often display spatial structures, commonly referred to as the "three-part structure" (a frontal structure, central bright core, and cavity – see Fig. 12). The frontal structure overlies the cavity, which contains the bright core. The core has been shown to be the eruptive prominence by comparing coronagraph and H-alpha observations. The cavity seems to be the flux-rope structure (Chen et al. [29]). Not all CMEs show the three-part structure either due to geometrical reasons or due to the nature of the source region (the eruption region may not have a filament). The cavity, if any, may be obscured by the overlying structure. If the CME is fast with respect to the local Alfven speed, it drives a shock. Such CMEs must have four-part structure, but the shock is often difficult to detect near the Sun. The circular shape of the outermost structure in halo CMEs may indeed be a manifestation of the shock (Sheeley et al. [30]).

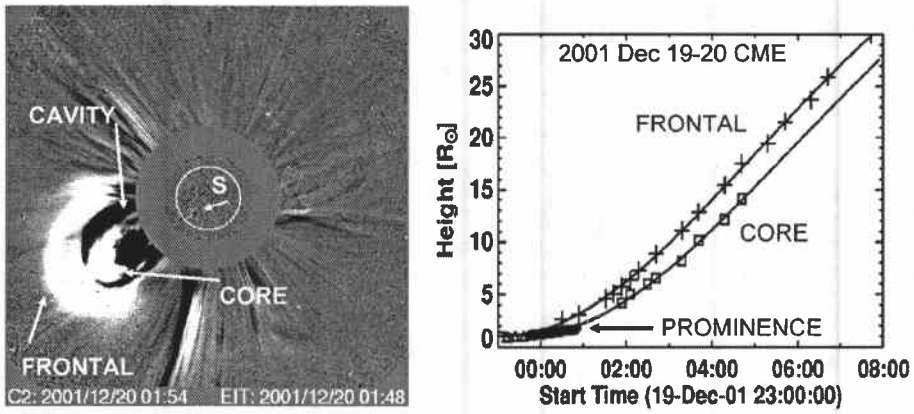

FIGURE 12. Three part structure of a SOHO CME (left) with the height-time plot (right). A prominence erupted on 2001 December 19, which became the core in white light the next day. The CME originated from the southeast quadrant of the Sun, where a faint post-eruption arcade can be seen. The cavity, frontal structure, and core are marked.

Halo CMEs: Some CMEs appear to surround the occulting disk of the observing coronagraphs and for this reason they are called halo CMEs (Howard et al. [31]). Halo CMEs are like other CMEs, except that they expand rapidly to be seen outside the occulting disk in projection. When the eruption region is on the visible side of the sun, they are called frontside halos; when the eruption takes place on the invisible side of the Sun, they are called backside halos. From an observational point of view, halo CMEs are referred as full (type F), asymmetric (type A), and partial (type P) halos (see Fig. 13). For F- and A-type halos, excess brightness is observed all around the occulting disk. For P-type halos, no excess brightness is seen above some fraction of the angular extent. A-type halos generally originate closer to the solar limb and they can be in front of, at, or behind the limb. F- and A-type halos are also simply referred to as halo CMEs and constitute ~3% of all CMEs (Gopalswamy [25]). Halos and partial halos together account for only ~11% of all CMEs. The Solwind coronagraph on board P78-1 satellite observed only ~20 full and partial halos (2% of all CMEs compared to the 11% here). Halo CMEs are studied as a class only after SOHO/LASCO started routinely observing them. Halo CMEs constitute an important population because they have important interplanetary consequences (see later).

5.3. Physical properties

The CME plasma is multithermal with the prominence core at ~8000 K and the outer structure at a few MK. Occasionally, CMEs may consist of flare ejecta with temperature exceeding 10 MK. The magnetic field in CMEs is not directly measurable near the Sun. The magnetic field in prominences is typically up to 30 G, while it can exceed 1000 G in the active region cores. The field strength in the outer corona is typically less than 1

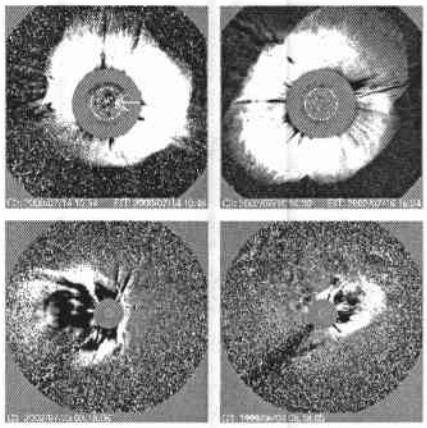

FIGURE 13. Examples of halo CMEs (clockwise): Frontside full halo, backside full halo, Asymmetric halo, and partial halo. The arrow in the frontside halo points to the eruption region on the Sun observed as a global disturbance in EUV images.

TABLE 3. CME properties from various coronagraphs (updated from Hundhausen [32])

Epoch	OSO-7 1971	Skylab 1973-74	Solwind 1979-85	SMM 1980,84-89	LASCO 1996-
FOV $R_\odot$	2.5–10	1.5–6	3–10	1.6–6	1.2–32
#CMEs	27	115	1607	1206	10541
V (km/s)	-	470	460	350	472
W (deg.)	-	42	43	47	45
M (10^{15} g)	-	6.2	4.1	3.3	0.4

G. The coronal cavity overlying the filament may also have field strengths higher than the overlying corona for pressure balance requirements.

5.4. Kinematic properties

The basic attributes of a CME are its speed, width, acceleration, and central position angle, all referred to the sky plane. Table 3 lists the epoch of operation, field of view (FOV in solar radii $R_\odot$), total number of CMEs observed, mean speed (V), mean width (W), mass (M in 10^{15} g) and the representative reference for spaceborne coronagraphs. Note that most of the properties are similar except for the low speed of the SMM CMEs and low average mass of LASCO CMEs. While the SMM speed anomaly could be an artifact of poor sampling (see Gopalswamy [25]), the LASCO mass is due to the large number of low-mass CMEs detected because of the high sensitivity.

CME Speed: The speed is normally determined from a linear fit to the height-time (h-t) measurements at a position angle, which appears to move the fastest. Quadratic fit to

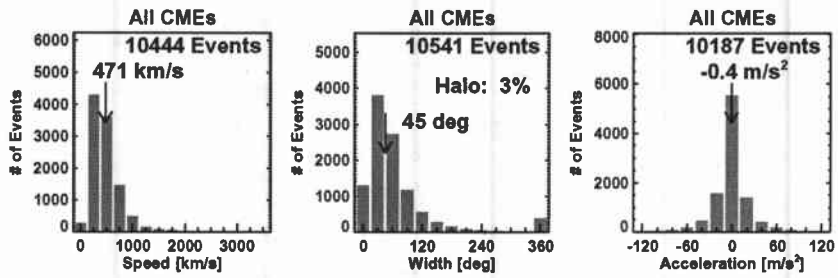

FIGURE 14. Distributions of speed, width, and acceleration of SOHO CMEs from detected from 1996 to 2005. Speed and acceleration were obtained from the height-time measurements. For some CMEs, height-time measurements could not be made for a small number of CMEs.

the h-t measurements gives the constant acceleration, which again is an approximation because the acceleration may also change with time. The measured sky-plane speed ranges from a few km/s to >3000 km/s (see e.g., Gopalswamy [25]; Yashiro et al. [33]), with an average value of 471 km/s (see Fig. 14). The average speed is similar to Skylab and Solwind values but significantly higher than the Solar Maximum Mission (SMM) value (350 km/s, Hundhausen [32]). The highest linear speed recorded by SOHO was ~3350 km/s and ~0.01% of CMEs had speeds exceeding 2500 km/s. Note that the number of CMEs at the highest speeds drops precipitously. This may be related to the maximum energy available in active regions that powers CMEs.

CME Width: CME angular span (also referred to as CME width) is measured as the position angle extent in the sky plane. For CMEs originating from close to the limb, the measured width is likely to be the true width. For CMEs away from the limb, the measured width is likely to be an overestimate. CMEs often show increase in width as they move out, so measurements are made when the width appears to approach a constant value. Earlier coronagraphs had smaller fields of view, so they might have underestimated the widths. The apparent angular width of CMEs ranges from a few degrees to >120°, with an average value of 45° (see Fig. 14). The average width (45°), determined only for CMEs with width < 120°, is also similar to pre-SOHO values. However, SOHO has detected a significant number of wide CMEs (~11%) and full halo CMEs (~3%). We did not include CMEs with W ≥120° because we do not know the actual width of such halo and partial halo CMEs due to projection effects. There is also a weak correlation between CME width and speed. Halo CMEs are about twice faster than average CMEs, which implies that they are generally wide.

Acceleration: The average acceleration within the coronagraphic field of view is almost zero, but it is actually speed-dependent. Most of the h-t plots fall into three types: accelerating, constant speed, and decelerating, indicating different degrees of propelling and retarding forces acting on CMEs (see Fig. 15). Since CMEs start abruptly, every CME has to accelerate from a zero speed to a finite speed early on. Most CMEs finish accelerating by the time they reach ~4 $R_\odot$ (Wood et al. [34]) except for some CMEs associated that continue to accelerate into the IP medium. Fast CMEs mostly decelerate (height-time profile (c) in Fig. 15) in the LASCO FOV. Far away from the Sun, the CME

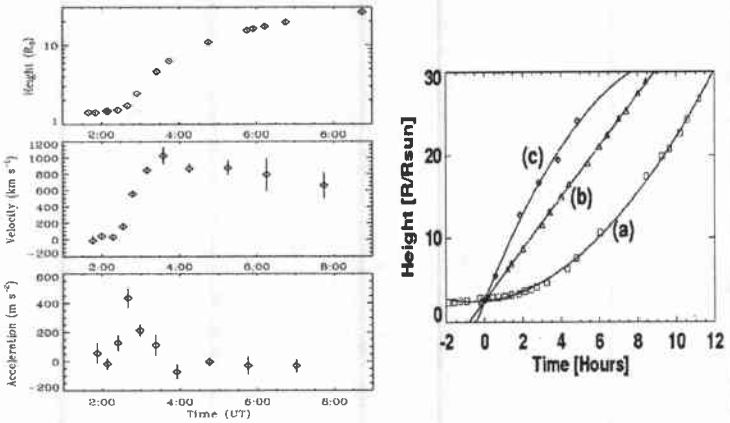

FIGURE 15. Acceleration time profile of a CME from Wood et al. [34] (left) and typical height-time plots of (a) accelerating, (b) constant speed and (c) decelerating CMEs (right) from Gopalswamy et al. [35].

speed tends to approach the background solar wind speed implying a strong coupling. This fact has been used in deriving empirical models to predict the arrival of CMEs and shocks at Earth.

CME Mass and Kinetic Energy: The width is a good indicator of the mass content of CMEs. The mass is estimated by determining the volume and the number of electrons in the CME with the assumption that the CME is a fully ionized hydrogen plasma with 10% helium. Like the width, the mass also changes during the early phase of the CME before stabilizing to a near-constant value. This constant value is used as the representative mass. CME mass ranges from a few times 10^{13} g to $>10^{16}$ g. The kinetic energy obtained from the measured speed and mass ranges from 10^{27} erg to $>10^{32}$ erg, with an average value of 5×10^{29} erg. Some very fast and wide CMEs have kinetic energies exceeding 10^{33} erg, generally originating from large active regions (see Gopalswamy et al. [36]). The average CME mass and kinetic energy are generally lower than the pre-SOHO values (see Table 3).

CME Latitudes: The latitude distribution of the central position angles of CMEs tends to cluster about the equator at minimum but broadens to cover all latitudes near solar maximum. The latitude distribution of CMEs depends on how closed-field regions are distributed on the solar surface (Hundhausen [37]; Gopalswamy [25]). Figure 16 shows a plot of the CME latitude as a function of time along with the maximum excursions of the heliospheric current sheet (a good indicator of the presence of closed field structures at high latitudes) for CMEs associated with prominence eruptions. Note that the CMEs shown are a subset of all CMEs because they are identified on the basis of prominence eruptions. The advantage is that the latitudes are known accurately from the prominence locations and hence the projection effects are minimal. CMEs occurring at latitudes higher than 60° are associated with the polar crown filaments, not associated with active regions or sunspots. On the other hand CMEs occurring at low latitudes may originate in active regions or filament regions.

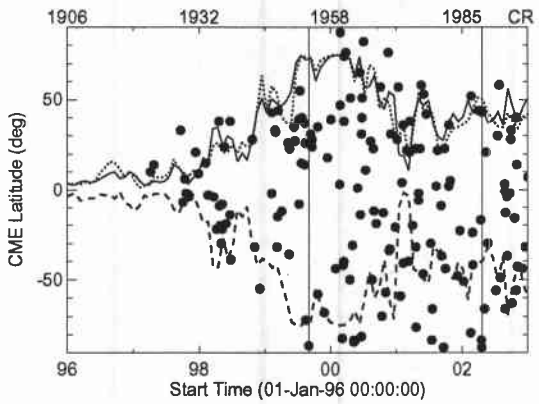

FIGURE 16. CME Latitudes identified from microwave prominence eruptions plotted as a function of time. The Carrington Rotation numbers are marked at the top (CR). The dotted and dashed curves represent the tilt angle of the heliospheric current sheet in the northern and southern hemispheres, respectively; the solid curve is the average of the two. The two vertical lines indicate the start and end of the high-latitude CME activities (from Gopalswamy [25]).

5.5. CME Rate

During solar minima, one CME occurs every other day. The rate goes up to several per day during solar maximum. The daily CME rate averaged over Carrington Rotations (27.3 days) was occasionally found to exceed 6/day (see Fig. 17), significantly higher than the pre-SOHO rate (~3/day). This is most likely due to the detection of fainter CMEs by LASCO. Solar cycle 23 started in May 1996, but the CME rate increased abruptly only in 1998 and remained relatively high through the middle of year 2002. There was a general decline after 2002, but the rate was still much higher than the solar minimum values. The large spikes in Fig. 17 are due to super active regions, which are prolific producers of CMEs. The CME rate shows a double peak, one toward the end of year 2000 and the other in the middle of 2002.

CME Rate and Sunspot Number: The two peaks in the CME rate are also observed in the sunspot number (SSN), but the amplitude and phase were significantly different. The SSN rate was highest during the first peak, while the CME rate was the highest during the second one. The SSN and CME rate are well correlated (see Gopalswamy et al. [38] and references therein), but the correlation is less than perfect. The differences may be traced to the multiple CME sources for CMEs. While the low-latitude (LL) CMEs are mainly associated with active regions (where sunspots reside), the high-latitude (HL) CMEs are not associated with sunspots. HL CMEs mostly occur during solar maximum, with rates occasionally comparable to the low-latitude (LL) rate. Thus solar activity measured in CME rate and SSN are expected to be not quite the same. A remarkable coincidence between the cessation of HL CMEs and the polarity reversal at solar poles has also been found (Gopalswamy et al. [39]).

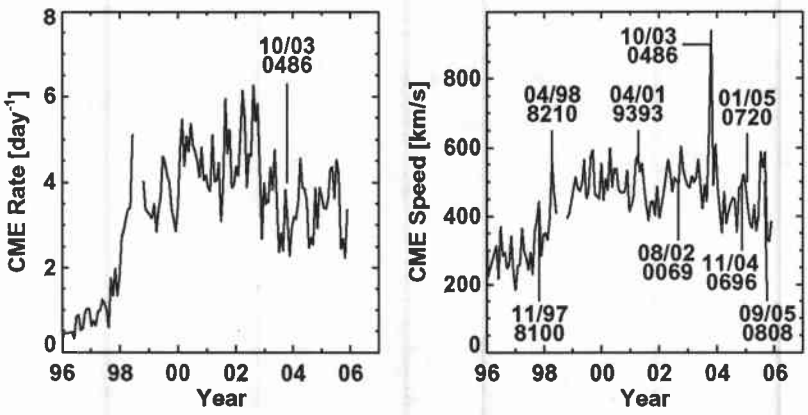

FIGURE 17. LASCO CME occurrence rate (left) and mean speed (right) from 1996 into 2005 averaged over Carrington Rotations. Some super active regions numbers and the month and year (mm/yy format) are also shown. The big spike in CME speed is due to CMEs in the Halloween 2003 period (10/03).

CME Rate and Mean Speed: The CME mean speed, obtained as the average speed of all CMEs occurring in a Carrington rotation shows a significant solar cycle variation (Fig. 17). The factor-of-two increase in the mean speed from minimum to maximum was inconclusive during cycle 22 (Webb & Howard [40]; Hundhausen [41]; Gopalswamy et al. [38]). The mean speed also shows the double peak mentioned above but the difference between the two peaks is not significant. The huge spike in 2003 is due to the famous Halloween events (October-November 2003) when an extraordinary set of fast CMEs occurred from three active regions (Gopalswamy et al. [42]).

CME Rate and Cosmic Ray Modulation: The high rate of HL CMEs just before the reversal of global solar magnetic field suggests that they may play also an important role in the modulation of galactic cosmic rays (GCR). SOHO results have conclusively shown the existence of a higher and more cycle-dependent CME occurrence rate (varying by factors up to 10) than pre-SOHO data indicated (Wagner [43]). Such higher rate is required for CMEs in the heliosphere to be effective in modulating GCRs (Newkirk et al. [44]). When the north pole of the Sun has positive polarity, GCRs enter the heliosphere along the poles, and hence directly encounter the HL CMEs propagating far into the heliosphere and deflect them. On the other hand, when the solar north pole has negative polarity, GCRs enter the heliosphere in the equatorial plane, so the LL CMEs effectively modulate them. CMEs take several months to more than a year to reach the termination shock, they are expected to modulate the GCRs over long time scales. The HL CMEs have minimal effect on GCRs during this epoch. This was quantitatively shown to be the case when the HL and LL CME rates were correlated against the GCR intensity (Gopalswamy [25]; Lara et al. [45]).

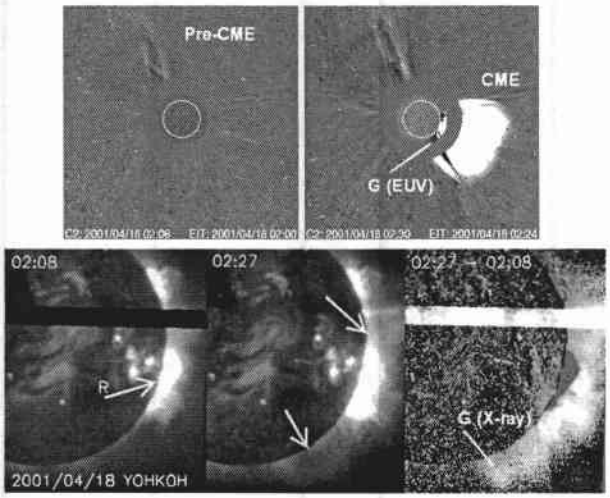

FIGURE 18. (top) The 2001 April 18 CME from behind the west limb with the EUV global disturbance marked G. When the Yohkoh image at 02:08 UT was subtracted from the one at 02:27 UT, we see a large-scale global (G) X-ray enhancement above the west and southwest limb. The CME originated from behind the limb at the position angle marked by R. Even in direct images, clear changes can be seen at locations pointed by arrows in the 02:07 UT image. Such enhancement was referred to as global engancement (Gopalswamy et al. [46]). The extent of the soft X-ray enhancement matches the extent of the EUV disturbance along the limb.

5.6. Multi-wavelength Observations of CMEs

Most of the observations presented above were obtained in white light by coronagraphs. The intensity of the Thomson-scattered photospheric light (in which the corona is imaged) depends on the number of electrons along the line of sight, so white light observations essentially sample the mass content of CMEs. Presence of the occulting disk in coronagraphs makes it difficult to observe the early phase of CMEs. Some narrower CMEs occurring near the disk center may not be observed at all. Therefore, one needs inner coronal imagers at other wavelengths such as H-alpha, X-ray, EUV, and microwave to get a complete picture of CMEs.

X-rays and EUV: Direct emission from the corona is imaged in X-rays and EUV, unlike in white light. Primary CME related signatures at these wavelengths are coronal dimming, ejected plasmoid, and post-eruption arcade formation. EUV wave transients (Thompson et al. [47]) have proven to be important signatures helpful in studying the early life of CMEs. Coronal dimming is interpreted as depletion of coronal material due to CMEs. Combined EUV and white light observations suggest that the coronal dimming corresponds to the depletion of the coronal material, which later becomes the CME in the coronagraph field of view (Gopalswamy et al. [48]; Thompson et al. [49]). Occasionally, global enhancement in X-rays was observed in the eruption region. This may be due to the excess emission caused by the compression of the corona at the periphery of fast CMEs. Fig. 18 shows an example of global enhancement during the

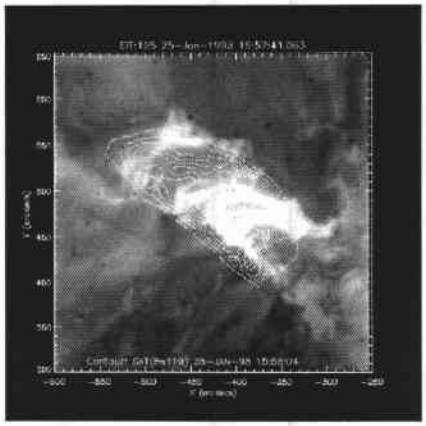

FIGURE 19. Soft X-ray intensity contours superposed on EIT (195 ï£¡ post eruption arcade following a CME on 1998 January 25. Note that some dark regions in EUV are bright in X-rays because of the differing temperature response in the two wavelengths.

2001 April 18 CME. The CME had a speed of 2465 km/s, which is evident when we compare the pre-CME image at 02:06 UT with the event image at 02:18 UT. In less than 24 minutes, the CME reached a height of ~ 5 $R_{\odot}$. The CME originated $\sim 30°$ behind the limb so the weak global enhancement was readily observed.

The ejected plasmoid is most likely the heated prominence core of CMEs. The CME leading edge is not seen in X-rays because the flare loops are usually much brighter. Under rare circumstances when there are no hot structures on the Sun, it is possible to detect the frontal structure (Gopalswamy et al. [50]). Arcade formation is a post-eruption signature (see, e.g., McAllister et al. [51]; Gopalswamy [52]; Tripathi et al. [53]) often used to identify the location and extent of an eruption. These are the X-ray counterparts of two-ribbon flares discussed before. Arcade formation is also observed in EUV, but not as complete as in X-rays. Figure 19 shows an arcade in X-rays and in EUV for the 1998 January 25 CME. An interesting result of this observation is that different loops of the arcade had different temperatures. Some of the darker loops in the EUV arcade were hotter, as evidenced by the fact that they were bright in X-rays. EIT waves seem to be fast mode MHD waves associated with solar eruptions and that they can become MHD shocks to produce metric type II bursts (Klassen et al. [54]). Under some circumstances, the EIT waves may be interpreted as shocks, especially when they have the "brow" structure (Gopalswamy [55]) and are closely associated with H-alpha Moreton waves and metric type II bursts.

Figure 20 illustrated the identification of the solar source of a CME by combining EUV and white-light images. The EUV images show the flare (bright feature) surrounded by the dimming region (the EUV manifestation of the CME). The white-light CME overlies the EUV dimming region.

Radio: In radio wavelengths, both thermal and nonthermal signatures of CMEs can be detected. Thermal emission depends on the temperature, density and magnetic field of the region as well as on the observing frequency. Nonthermal emission depends on

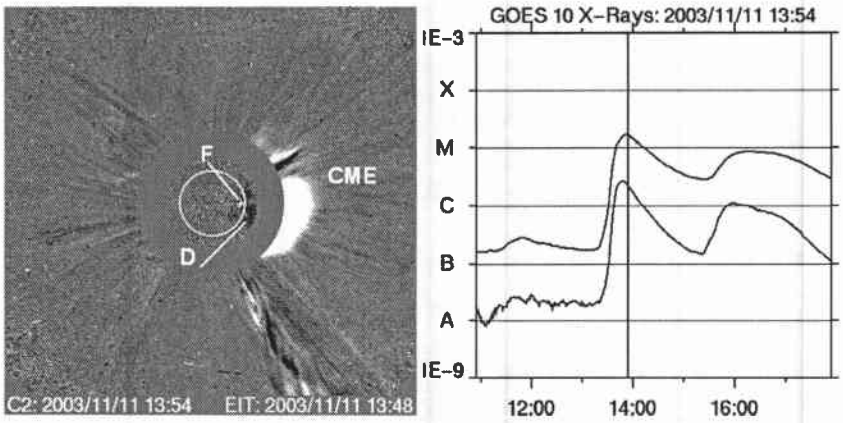

FIGURE 20. Solar origin of the 2003 November 11 CME revealed in EUV image. Radially below the white light CME, an extended dimming region (D) surrounds the flare location (F) seen as compact bright emission (an M-class flare as shown as GOES light curve in the right). The vertical line on the GOES plot marks the time of the white light image. The second peak in the GOES light curve is from another eruption in the east limb, not related to the CME in question. Both the white light and EUV images are difference images (a preceding image was subtracted from the shown image) that show the changes better. This figure illustrates how inner coronal images are helpful in studying the early evolution of CMEs.

quantities such as the density and energy of the nonthermal electrons. A number of mechanisms operate in producing thermal and nonthermal radio emission, so a careful identification of the mechanism is crucial in using the radio technique for CME studies.

Filament/prominence eruptions, post-eruption arcades (Hanaoka et al. [56]; Gopalswamy et al. [57]) and even coronal dimming can be studied using microwave images (Gopalswamy [58]). Filament eruptions in microwaves provide quantitative information on the eruptive process. Coronal dimming in microwaves is somewhat difficult to observe because the coronal structures are optically very thin. Nevertheless, the microwave dimming has been shown to be consistent with X-ray dimming, confirming the depletion of material from the corona (Gopalswamy [52]).

Since CMEs are denser than the ambient corona, they must be optically thick at low metric frequencies. Sheridan et al. [59] detected changes in the radio streamer associated with a slow CME observed by Skylab. Gopalswamy & Kundu [60] imaged the thermal free-free emission from a CME 73.8, 50 and 38.5 MHz. In addition to the CME body, density depletions in the aftermath of CMEs have also been detected at long wavelengths (Ramesh & Sastry [61]; Kathiravan & Ramesh [62]). Recent images made by the Nancay radioheliograph show radio structures that correspond to the frontal structure of CMEs (Maia et al. [63]). The main difficulty in imaging thermal emission from CMEs at metric frequencies is the simultaneous occurrence of nonthermal bursts that can easily mask the thermal emission.

As discussed in the section on flares, electrons escaping from the region of eruption along open field lines produce type III bursts; electrons confined to shock fronts produce type II bursts; those trapped in moving coronal structures type IV bursts. Type II and

TABLE 4. Hierarchical relationship between CME properties and the wavelength range of type II bursts

	All	m	DH	mkm	km
Speed (km/s)	487	610	1115	1490	539
Width (deg)	45	96	139	171	80
Halos (%)	3.3	3.8	45.2	71.4	17.2
Acceleration (m s^{-2})	-2	-3	-7	-11	+3

type IV bursts are closely associated with CMEs. Detailed knowledge on the magnetic structures carrying nonthermal electrons with energies exceeding 1 MeV was available before the detection of white light CMEs (see, e.g., Schmahl [64]). Gopalswamy & Kundu [65] tracked a moving type IV burst for several solar radii at three frequencies and found that the radio source moved roughly with the speed of the associated white light CME. Stationary type IV bursts occur when energetic electrons are trapped in post-eruption arcades. The frequency range of stationary type IVs is from microwave frequencies to a few MHz. The lowest frequencies suggest that occasionally the post-eruption arcades extend to a few solar radii. CMEs associated with such low-frequency type IV bursts have been shown to be among the fastest of CMEs (Gopalswamy [66]).

Type III bursts extend from high frequencies corresponding to the electron densities in the flare site to KHz frequencies corresponding to the plasma frequency in the vicinity of the observing spacecraft. When CMEs drive shocks, they produce type II radio bursts due to electrons accelerated at the shock front. Type II bursts are also observed over similar frequency range or in terms of wavelengths, from metric (m) to kilometric (km) wavelengths. In addition to the traditional metric and kilometric wavelengths, the Wind spacecraft provided opportunity to observe the type II bursts in the Decameter-hectometric (DH) regime also. These observations provided a complete picture of the type II bursts and their relation to CMEs. Since these plasma frequencies prevail at various layers between the Sun and the observer, they provide opportunity to probe the interplanetary medium as well as the energy sources (electron beams, shocks). The decade-long overlap between Wind/WAVES and SOHO observations enabled a fresh look at the CME-type II relationship. Gopalswamy et al. [67] found a hierarchical relationship between the CME kinetic energy (speed, width) and the wavelength range of type II radio emission (see Table 4). The CME kinetic energy essentially decides the wavelength range of type II bursts because the speed, width, and deceleration progressively increase for CMEs associated with m, DH and m-to-km type II bursts. The only exception was the purely km type II bursts, which were associated with accelerating CMEs, suggesting shock formation occurs at large distances from the Sun.

Another interesting result was that most of the CMEs with m-to-km type II bursts were also associated with SEP events (same shock accelerates electrons and protons). In fact, the properties CMEs associated with m-to-km type II bursts and large SEP events were identical.

In-situ observations: CMEs of higher kinetic energy propagate far into the IP medium. It has been estimated that ~10% of CMEs propagate as distinct structures into the IP medium (Gopalswamy [25]). Near the Sun, CMEs are observed mainly as density

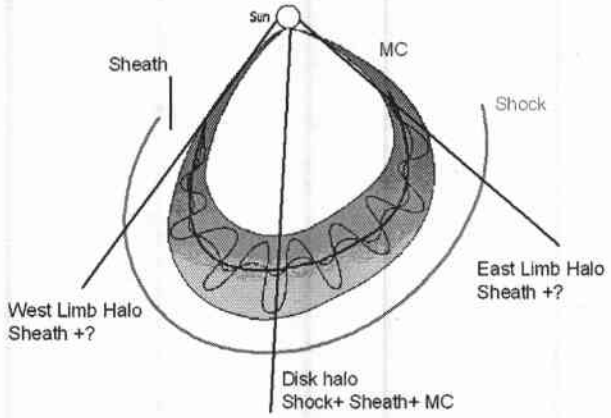

FIGURE 21. Sketch of a magnetic cloud (MC) with its flux-rope structure (note the helical field lines wound around the cloud axis) driving a shock. The compressed region between the MC and shock is known as the sheath. Three Sun-Observer lines are drawn to illustrate that the MC structure is seen only when the nose of the cloud heads towards the observer. MCs heading at large angles to the Sun-Observer line are observed as interplanetary CMEs without flux-rope structure.

structures. On the other hand the magnetic field strength is a key identifying parameter for the IP counter parts of CMEs (ICMEs). Magnetic clouds are a subset of ICMEs that have an enhanced magnetic field, smooth rotation, and low plasma beta (Burlaga et al. [68]). Figure 21 shows a sketch of an MC. Overall ~1/3 of the ICMEs are observed as magnetic clouds. According to the geometry shown in Fig. 21, CMEs originating within 30° from the Sun center are likely to have their nose reaching Earth. CMEs originating at greater central meridian distance will have their flanks impacting Earth and hence may not be observed as MCs. The number of MCs relative to the number of ICMEs varies by a large factor. This is because of other factors such as the strength of the global dipolar field of the Sun which forces CMEs towards the equatorial plane, so more ICMEs appear as MCs. The leading field of the MC and the sheath field have some relation to the global field of the Sun and the active region field from which the associated CME originates. Unfortunately, there is no reliable measurement of vector magnetic field in the corona, so we cannot make accurate correspondence between CME features near the Sun and at 1 AU.

The location of the solar sources of MCs has definite solar-cycle variation. MC-associated CMEs originate from very close to the Sun center (within 30° in longitude and latitude), and have a slight western bias (the average location is W07). The MC sources occur at higher heliographic latitudes during the rise phase of the solar cycle compared to the maximum and declining phases, mimicking the butterfly diagram.

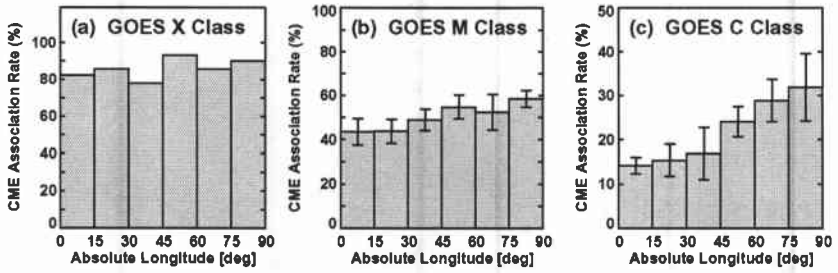

FIGURE 22. CME association rate as a function of longitude of flare longitude for GOES X-class (a), M-class (b) and C-class (c) flares during 1996-2005. All X and M-class flares are included. C-class flares with peak flux $\geq$ C3.0 are included. (adapted from Yashiro et al. [72]).

5.7. CMEs and Flares

Flares occur with and without CMEs. Some flares also are associated with mass motions in the form of jets. Early statistical studies (see, e.g., Kahler [69]) showed that $\sim$ 40% of CMEs were associated with H-alpha flares and almost all flares (90%) with H-alpha ejecta were associated with CMEs. Thus the "mass motion" aspect of flares seems to be critical for a flare to be associated with CME. Studies on temporal correspondence between CMEs and flares have concluded that CME onset typically precedes the associated X-ray flare onset by several minutes (Harrison [70]). This observational fact is considered to be a serious difficulty for flares to produce CMEs (Hundhausen [41]). Recent observations indicate that CMEs accelerate impulsively until the peak of the soft X-ray flare. There is also weak correlation (r = 0.53) between soft X-ray flare intensities and associated CME energies (Hundhausen [41]; Moon et al. [71]). The association rate between CMEs and flares steadily increases with flare size becoming nearly 100% for high X flares. There is also a center-to-limb variation of CME association rate with flare location on the solar disk. Figure 22 shows that almost all X-class flares are associated with CMEs irrespective of their location on the disk. For M and C flares, the CME association rate is $\sim$15% and 50% less for disk flares compared to limb flares. Assuming that the limb rate is the actual rate of association, we see that about half of the C-flare associated CMEs might have been missed by the SOHO coronagraphs.

When soft X-ray flares are used to make the flare-CME association, one can always find a soft X-ray flare associated with a CME if the CME occurs on the visible disk. On the other hand as Fig. 22 shows there are even X-class flares and many M-class flares that are not associated with CMEs. In other words, flares do occur independent of CMEs, but CMEs do not erupt independent of flares. We can say that CMEs is one of the ways flares happen, but there are other ways also. For example, confined flares happen in compact region with no mass motion. Yashiro et al. [73] found that flares with and without CMEs have different frequency distributions: the power laws in peak flux, fluence, and duration are all steeper for CMEless compared to flares with CMEs. For example, CMEless flare fluence has a power law index of 1.79 compared to 2.47 for flares with CMEs (see

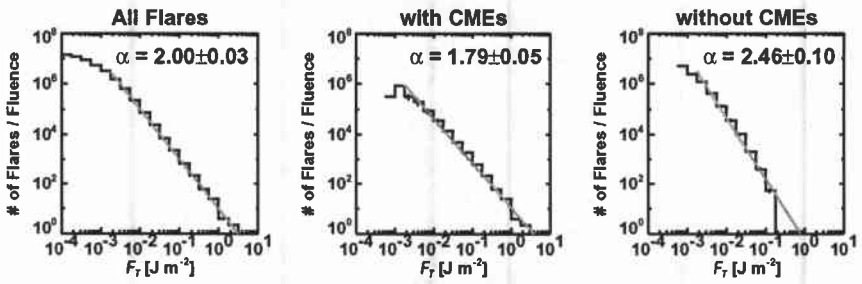

FIGURE 23. Frequency distribution of flare fluence for all flares (left), flares with CMEs (middle) and the CMEless flares (right). The distributions follow are power laws with indices 2.0, 1.79, and 2.46, respectively.

Fig. 23). A power-law index > 2.0 is needed for flares to contribute to coronal heating (Hudson [74]). Combined with the fact that CMEless flares are generally hotter than flares with CMEs (Kay et al. [75]), tiny flares might heat the corona.

5.8. Prominence Eruptions

It is known for a long time that most of the CMEs are associated with prominence eruptions (Munro et al. [76]) and the reverse is also true (Gopalswamy et al. [57] and references therein). Both quiescent prominences (located in the quiet Sun) and active prominences (located in active regions) erupt and become part of CMEs. For this reason, it is not a good idea to classify CMEs as flare associated and prominence eruption associated. The flares associated with active prominence eruptions are generally larger. When prominences erupt, part of the material usually falls back to the surface, the remaining going into the IP medium with the overlying structures. Prominence eruptions not associated with CMEs have their motion predominantly in the transverse direction, while those associated with CMEs have a radial motion. There are also intermediate cases where a "streamer change" is observed with partial eruptions. One of the earliest signatures of CMEs is known to be small scale changes in prominences (known as filament activation) minutes to hours before CME onset. There seems to be a critical height the prominences have to attain before they erupt.

5.9. CME Models

The largest kinetic energy measured in a CME is a little more than 10^{33} erg (Gopalswamy et al. [36]). Coronal volume of a large active region is $\sim 10^{31}$ cm^3. To supply the necessary kinetic energy, the eruption region should convert $\sim$200 G. Such magnetic field strengths are readily observed in the corona, but what is needed is the free energy stored in the magnetic field in the form of coronal currents flowing along field lines. There is ample evidence in vector magnetograms about the presence of such currents.

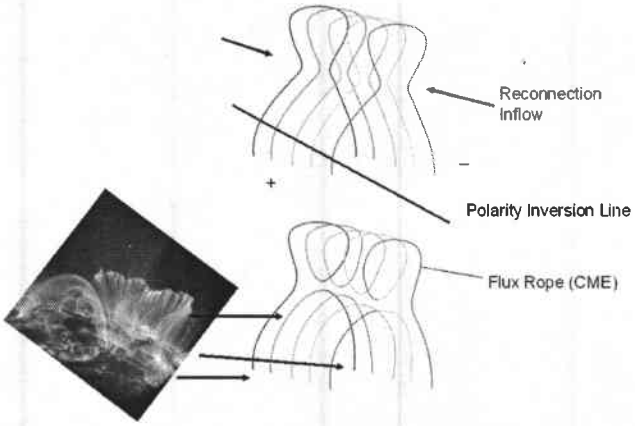

FIGURE 24. A set of 5 closed field lines overlying a polarity inversion line reconnect near their top producing a set of four closed filed lines (which are potential) and the flux rope. A TRACE image is also with a post-eruption arcade resembling the potential field lines. Courtesy: G. Holman

The magnetic potential energy in an active region has been taken to indicate the amount of free energy that can be stored in the region. Typically about half of the total energy is taken to be in the potential fields and the other half is in the coronal currents (free energy).

Most of the filaments observed on the Sun seem to be non-potential structures because the field lines are roughly parallel to the polarity inversion line. X-ray sigmoids are thought to be non-potential structures. Coronal cavities observed in white-light, X-ray, and EUV appear to overly filaments and are thought to be the flux rope that erupts as observed in the interplanetary medium. It is not clear whether the flux rope emerges from under the surface, formed as a result of slow evolution before eruption, or formed during the eruption. Figure 24 illustrates the formation of a flux rope as a result reconnection during eruption. Flux emergence, flux cancellation, shear motion, and other photospheric flows are the pre-eruption evolutions that stress the magnetic fields thereby storing the energy in the pre-eruptive structures. The storage cannot proceed indefinitely, so a stable equilibrium of the stressed magnetic field may no longer be possible at some stage, when the structure erupts with its plasma. Small-scale energy releases such as small-scale heating near filaments, filament activation and nonthermal radio bursts are thought to be indicative of impending eruption. CME initiation models are concerned with how the energy is stored in the coronal fields and what triggers the release of this energy. The main difficulty is in the measurement of coronal magnetic fields, which is virtually non-existent except for radio observations and some recent infrared observations.

A flux rope is central to many CME models. MHD computations of CME source configurations have shown that flux cancellation can lead to the formation and eruption of flux ropes (e.g., Lin et al. [77]; Amari et al. [78]; Linker et al. [79]). In these models, the flux cancellation is the reconnection process that leads to the release of the flux rope into the interplanetary medium. Some models require a reconnection overlying the eruptive structure embedded in a multipolar configuration as in the breakout model

(Antiochos et al. [80]). Macroscopic reconnection can also inject poloidal flux to set the flux rope into motion (Chen [81]). Moore & Sterling [82] conclude that CMEs involve the explosion of sheared core field in active regions assisted by internal and/or external tether cutting that leads to the erupting flux rope. Observation of flux ropes in the interplanetary medium (magnetic clouds) is a strong motivating factor in considering an initial flux rope configuration. Furthermore, there is a strong possibility that all CMEs observed in the interplanetary medium may have flux rope structures.

Once the CME is launched, it propagates into the outer corona and IP medium. CME propagation can be described analytically using the propelling and retarding forces acting on CMEs in the interplanetary medium (Schmidt and Siscoe in Forbes et al. [83]). Analytical calculations were facilitated by the empirical relation between CME speed and acceleration (Gopalswamy et al. [84]). Comparison of the velocity versus distance plots from analytical models and an MHD simulation model (Riley et al. [85]) yields satisfactory results suggesting that understanding the transport physics involving flux rope expansion, generalized buoyancy, gravity, and interplanetary drag is within our reach. This is an important aspect of CME research because it has the practical implications for the prediction of CME arrival at a given location in the heliosphere.

6. SOLAR ENERGETIC PARTICLES

Solar energetic particles (SEPs) are so called because of their high energy, solar origin, and behavior as single particles. SEPs consist of electrons, protons, alpha particles, 3He nuclei and heavier ions up to Fe. SEPs are observed as an increase in the particle flux as detected by a particle detected in space (see Fig. 25). Occasionally, protons penetrate Earth's atmosphere causing air showers and the resulting secondary neutrons are observed on the ground by neutron monitors. In fact the discovery of SEP events was made by Forbush [86] in the neutron monitor records from 1942. These events are known as SEP events with ground level enhancement (GLE). Energetic particles are also observed with high intensities when IP shocks are intercepted by spacecraft. These particles are same as SEP events, but accelerated locally and are known as energetic storm particles (ESPs). Observation of ESPs is considered as the direct evidence for particle acceleration by interplanetary shocks. Electrons up to a few MeV and protons up to a few GeV are observed in near-Earth space. SEPs also carry important information about the acceleration region near the Sun. We already talked about accelerated electrons and ions causing flare-related emission at various wavelengths. These particles are generally referred to as interacting particles as opposed to the SEPs, which escape into the interplanetary medium and hence called the escaping particles.The relation between the two populations is not fully understood.

Currently there are two basic processes by which SEPs are thought to be accelerated: the flare reconnection process and acceleration at the shock fronts. The purely flare-associated SEP events have been classified as impulsive (short-lived) events as opposed to the "gradual"(long-lived) events from CME-driven shocks (see, e.g. Lin [87]; Reames [88]). Properties of impulsive and gradual events are listed in Table 5. While this classification has been useful, it must be pointed out that SEP-associated CMEs are also associated with intense flares, so it is often difficult to untangle the contributions

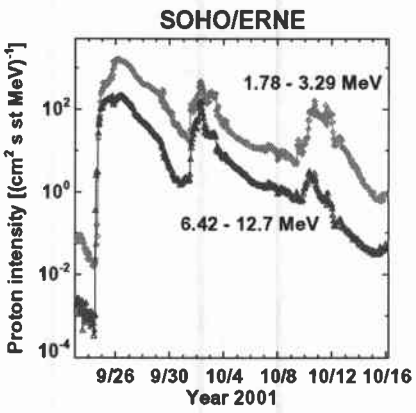

FIGURE 25. Proton intensity during a CME event on 2001 September 24 in two energy channels. Note that the proton intensity suddenly goes up by a factor of 10^4 in a short time. The intensity remains elevated for several days before the occurrence of two additional events. The largest peak in the lower energy channel occurs about a little more than one day, which corresponds to the arrival of the CME-driven shock at the observing spacecraft. The shock associated part of the particle event is known as the energetic storm particle event.

from flare and shock sources (Cliver [89]). High charge states of Fe (20) in some SEP events suggest that the particles must have originated at very high temperatures exceeding several MK. From X-ray observations we know that the only place in the solar atmosphere where such high temperatures exist is the flare plasma. High charge states typically occur in impulsive SEP events (Reames [88]). In some large SEP events the Fe charge state is only $\sim$14, which means the SEPs originated at normal coronal temperature. This happens when a CME-driven shock accelerates coronal material. The simple picture of impulsive and gradual events needs to be modified as recent observations demand. Torsti et al. [90] recently studied a set of SEP events during solar maximum (1999-2000) and found that most of them showed an overabundance of 3He suggesting that impulsive, flare-type (reconnection) processes always participate in the production of SEPs. They suggest that the canonical value for the ratio 3He/4He should be 0.015 rather than the 0.0005 assumed for gradual SEP events (see Table 5). Similarly, higher heavy-ion charge states are observed in gradual SEP events. As far radio bursts, it was initially thought that in gradual SEP events, electrons produced in the reconnection behind the CME may not have access to open field lines. In fact the type III bursts associated with SEP events occur in a large group lasting for tens of minutes. In impulsive events, type III bursts occur isolated or in small groups whereas they occur in large groups in gradual events (see e.g., Reiner [91]). Finally, the density ratio Fe/O is not constant, but is energy dependent with bimodal trend at higher energies (see Tylka & Lee [92]). In order to explain such energy dependent spectra and abundances, one has to consider the evolution of shock geometry with respect to the Sun-observer field line as the shock propagates from state and the contribution from the concomitant and/or preceding flares. Cliver & Ling [93] have recently provided evidence supporting the

TABLE 5. Properties of Impulsive and Gradual SEP Events with suggested modifications in square brackets

	Impulsive	Gradual
Particles	Electron Rich	Proton Rich
3He/4He	~1	~0.0005 [~0.015]
Fe/O	~1	~0.1
H/He	~1	~100
QFe	~20	~14 [>14]
Duration	Hours	Days
Longitude Cone	<30°	~180°
Radio Type	III, (II)	II,IV [II, IV, III]
X-Rays	Impulsive	Gradual
CMEs	none [often]	96% [100%]
Events/Year	~1000	~10

dominant shock contribution to the SEP intensity, the flare contribution being an order of magntitude smaller at energies at least up to 30 MeV.

Recent studies indicate that preceding events may influence the later events: flare particles from a sequence of preceding flares may be present in the inner heliosphere and get accelerated by CME-driven shocks (Mason et al. [94]). When CMEs occur in rapid succession from the same neighborhood, some of the SEPs produced by one CME may become seed particles to the next CME (Kahler [95]). Presence of preceding CMEs means disturbed conditions in the coronal and IP medium through which later CMEs propagate: density, flow velocity, magnetic field strength, magnetic field geometry, turbulence, and solar wind composition may be different compared to normal solar wind conditions (Gopalswamy et al. [96]). Large SEP events with preceding wide CMEs within a day from the same active region tend to have higher intensity (Gopalswamy [25]). The average and median time separations between the primary and preceding CMEs were found to be 11 and 12 h, respectively (the range is <1 to 21 h). The average time separation is much smaller than the typical duration of large SEP events, so event-averaged quantities should be different for cases with and without preceding CMEs. Strengthening of the shocks when propagating through the dense parts of preceding CMEs, trapping of particles in the closed loops of preceding CMEs, and reconnection between the preceding and following CMEs were suggested as possible mechanisms for the increased efficiency of particle acceleration (Gopalswamy et al. [98]). Recent numerical simulations support shock strengthening (Schmidt & Cargill [99]).

The two-class picture has another modification in terms of CME association also: during some impulsive SEP events CMEs and metric type II bursts have been observed. Studying a sample of 38 impulsive SEP events, Yashiro et al. [100] found that ~40% of impulsive SEP events were associated with CMEs. This rate is much larger than the occasional association reported in an earlier study (Kahler et al. [101]). However, only 13% of the impulsive SEP events were associated with metric type II radio bursts. The CMEs associated with impulsive SEP events were significantly slower (median speed of 613 km/s) and narrower (49°) than those of CMEs associated with large gradual SEP events (1336 km/s, 360°), but faster than the general population of CMEs. In fact in

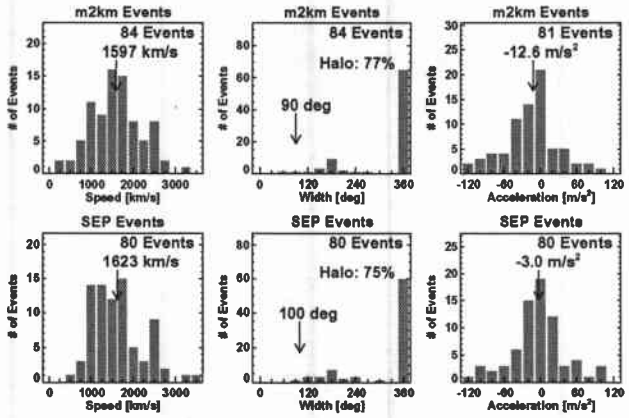

FIGURE 26. Speed, width, and acceleration distributions of CMEs associated with mkm type II bursts (top) compared with those associated with large SEP events. The averages of the distributions are shown on the plots. For CME widths, only non-halo CMEs were considered because we do not know the true width of halo CMEs.

the case of the largest impulsive event of cycle 23, there was a fast and wide CME associated with it, similar to a gradual SEP event (Gopalswamy et al. [102]; Tylka et al. [103]). Thus, we retain type II bursts in the impulsive SEPs column in Table 5 as (II), we need to change the CME association from "none" to "often".

The close connection between gradual SEP events and metric-to-kilometric (mkm) type II bursts confirms that the same CME-driven shock accelerates electrons (to produce type II bursts) and ions (observed at SEP events). In fact, the speed, width and acceleration distribution of CMEs associated with SEPs and mkm type II bursts are nearly identical (see Fig. 26). About three-quarters of the associated CMEs are also halo events. Furthermore, the number of mkm type II bursts and SEP events are also similar with slight differences due to the different source requirements for mkm and SEP-associated CMEs (SEP source needs to be magnetically connected to the observer so western hemispheric eruptions are favored). Thus the close association between gradual SEP events and CME-driven shocks is amply demonstrated. In conclusion, one can say that the number of modifications introduced in Table 5 is not enormous and the two-class picture is still useful in understanding various situations in which SEPs arise.

7. ENERGETIC PHENOMENA AND SPACE WEATHER

Space Weather refers to the conditions in the space environment that is hazardous to space or ground based technological systems or to human health or life. SEPs, geomagnetic storms, and ionospheric storms are some of the space weather effects directly linked to the energetic phenomena discussed above. Geomagnetic storms are caused by CMEs and stream interaction regions impinging on Earth's magnetosphere and further impacting the ionosphere. Energy coupling between a solar wind structure

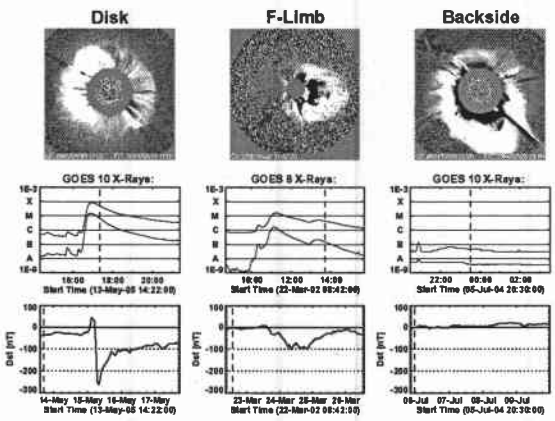

FIGURE 27. Geomagnetic activity level following disk, limb and backside halo CMEs.

and Earth's magnetosphere happens when the former has a southward magnetic field component. When the opposite fields come together, reconnection takes place, allowing the solar wind plasma enter the magnetosphere, thus initiating a storm.

7.1. CMEs and Geomagnetic Storms

Geomagnetic storms are disturbances identified in the horizontal component of Earth's magnetic field as measured by a set of magnetometer stations near Earth's equator. The global value of the average disturbance is known as the Dst index, which serves as a measure of the strength of the geomagnetic storm. Geomagnetic storms are classified as intense (Dst $\leq$ -100 nT), moderate (-100 nT $<$ Dst $\leq$ -50 nT), and weak (Dst $>$ -50 nT). A geomagnetic storm is caused whenever an interplanetary structure impinges upon Earth's magnetosphere. We have already mentioned that CIRs can cause moderate storms. CMEs cause the severest of storm. The ability of an interplanetary structure in causing a geomagnetic storm is known as its geoeffectiveness. Frontside halos are the most geoeffective because they directly impact Earth. Non-halos can also be geoeffective if they have appropriate speed and width. A recent study found that most (71%) of the frontside halos produced moderate or intense geomagnetic storms (Gopalswamy et al. [104]). The overall strength of the storms declines as the solar source location of the CMEs on the Sun changed from the disk to limb to backside, as illustrated by the three examples in Fig. 27. There is also a solar cycle variation of CME geoeffectiveness: strongly geoeffective halos are confined only to the maximum and declining phases, consistent with the high mean speed of CMEs during these phases (see Fig. 17). Non-geoeffective halos generally had lower speed, predominantly originated from the eastern hemisphere, and had a greater central meridian distance.

The arrival of a CME-related disturbance at Earth's magnetosphere is marked by a sudden increase in the Dst index due to the compression of the magnetosphere. This

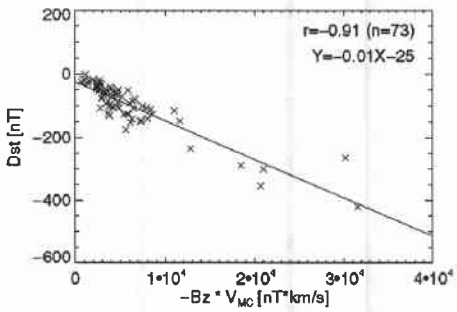

FIGURE 28. Scatter plot between Dst index and the product of MC speed and -Bz for MCs detected during 1995-2005. The correlation coefficient and regression line are shown on the plot.

positive excursion (see the first example in Fig. 27) is referred to as storm sudden commencement, which happens whenever the CME drives a shock. The storm occurs depending on where behind the shock does the interplanetary magnetic field turns south. If the shock sheath region has a Southward field (Bs), the storm starts immediately after the shock. If the southward field is contained in the front or back of the driving CME, then the storm occurs whenever the Bs structure arrives at the magnetosphere. The flux-rope structure in CMEs implies a specific magnetic structure and hence it is likely to contain Bs under most circumstances.

7.2. Magnetic Clouds and Geomagnetic Storms

A single white-light CME observed near the Sun may result in a shock, sheath, and MC at 1 AU. A CME can be geoeffective (because of the sheath) but not the associated MC. Since most MCs have been shown to be flux ropes, they almost always cause a storm because either the front or the rear section of the cloud contains Bs. Overall, two-thirds MCs are geoeffective whether one starts from MCs or geomagnetic storms. This is consistent with the geoeffectiveness rate of halo CMEs because CMEs associated with most of the MCs are halo CMEs. The non-geoeffective or weakly geoeffective MCs are generally slow, have low magnetic field strength, and occur mostly during the rise phase of the cycle.

The CME speed and the strength of the magnetic field it contains primarily decide the intensity of the geomagnetic storms: Fig. 28 shows that the product of MC speed (V_{MC}) and the 1-AU field strength in the Z direction (-Bz is southward) has the best correlation with Dst index (correlation coefficient = 0.91). The product of CME speed and -Bz also has a high correlation with Dst, which suggests that if we can measure Bz near the Sun in addition to the CME speed, we have a way of predicting geomagnetic storms.

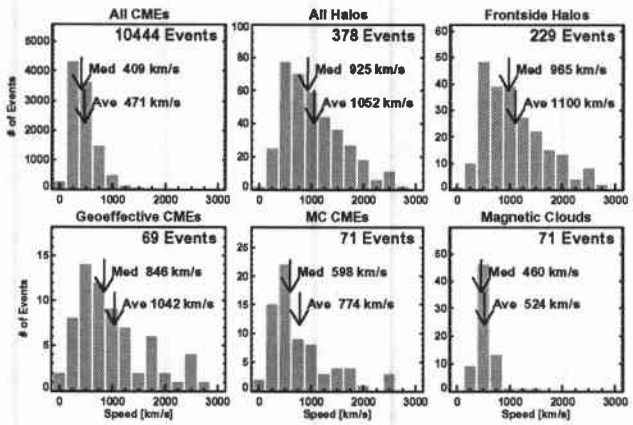

FIGURE 29. Speed distributions of all CMEs, all halo CMEs, frontside halos, geoeffective CMEs, and MC-related CMEs, compared with that of MCs. Only those MCs with corresponding white-light CMEs are included in the last panel.

Figure 29 compares the speeds of geoeffective CMEs, halo CMEs, and SEP-producing CMEs. The MC-associated CMEs are nearly twice as fast as the general population of CMEs (774 km/s vs. 471 km/s). The average speeds of halo CMEs (1052 km/s), front-side halos (1100 km/s) and geoeffective CMEs (1042 km/s) are similar to one another. The speed distributions of halos, geoeffective CMEs and MC-related CMEs have the same shape because we expect a high degree of overlap among them. We do expect differences because not all geoeffective CMEs evolve into magnetic clouds and not all MCs are highly geoeffective. The MC speed distribution (measured at 1 AU) is the narrowest with an average speed (524 km/s) that is slightly higher than the slow solar wind speed. This is because the CMEs start out with high speeds, but by the time they propagate to 1 AU, they slow down due to the strong coupling with the solar wind resulting in a narrower distribution at 1 AU (Lindsay et al. [105]; Gopalswamy et al. [84]).

7.3. Sun-Earth Transit of Geoeffective CMEs

The change in speed of CMEs observed near the Sun and at 1 AU can be quantified as an interplanetary acceleration so that empirical models can be developed to predict the arrival times of CMEs and shocks at Earth (Gopalswamy et al. [106] and references therein). Since it is difficult to measure the speed of the cavity for Earth-directed CMEs, the sky-plane speed is used. There are two ways the CME speed is quantified. One is to measure the sky-plane speed at the fastest moving segment of the CME and get the space speed by correcting for projection effects (Xie et al. [107]). The speed measured near the Sun corresponds to the leading edge or frontal structure of the CME, assumed to the same as the flux rope. The other is to measure the expansion speed, which is

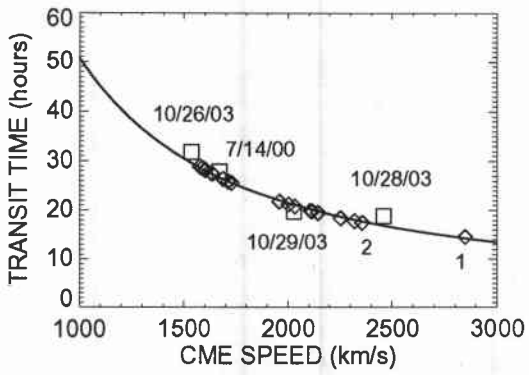

FIGURE 30. The time taken by CME-driven shocks to arrive at Earth after they lift off from the Sun. The diamonds represent historical events for which there is no CME observation, but the speed is inferred. The solid line is the empirical shock arrival model by Gopalswamy et al. [36]. The squares represent data points for which CME speed and shock arrival times are available from spacecraft measurements.

related to the radial speed (Schwenn et al. [108]) depending on the width of the CME. At 1 AU, the MC or ejecta speed is used to determine the speed change. Gopalswamy et al. [36] arrived at an empirical shock arrival model as shown in Figure 30. The model gives the shock arrival time (T) at Earth as a function of the CME initial speed (V) near the Sun as $T = aV^b+c$, where a=151.002, b=0.998625, and c=11.5981. T ranges from 50 h for 1000 km/s CMEs to 13.5 h for 3000 km/s CMEs. Also shown are some fast-transit shocks from SOHO. The transit times of historical fast-transit events, whose CME speeds are inferred from the above formula, are also shown for comparison. The transit-time formula suggests that the Sun-Earth transit times of shocks may not exceed ~12 h, because the number of CMEs with speeds exceeding 2500 km/s drops precipitously. It appears that we may have at least ~half-a-day lead time for shock arrival at Earth because not many CMEs have been observed with speeds greatly exceeding 3000 km/s. This speed limit on CMEs may be related to the amount of free energy available in active regions. No sunspots have been observed with field strength exceeding ~5000 G, so there is only a finite amount of energy released in active regions.

8. CONCLUDING REMARKS

In the overview presented in the preceding sections, it is clear that the magnetic field generated in the Sun's interior and brought to the surface is ultimately responsible for the most energetic phenomenon in the heliosphere. CMEs and flares derive their energy from the magnetic fields on the solar surface. Flares and CMEs also produce varying impacts on Earth via electromagnetic and particle radiations. High speed streams and the associated stream interaction regions owe their origin to a different type of magnetic field state on the Sun: the open field lines. When high speed streams collide with the low-

speed streams ahead, they produce the interaction regions. Interestingly, the interaction regions also appear as bumps in the interplanetary magnetic field, somewhat similar to the magnetic clouds, but with different thermal properties. The interaction regions can also drive shocks and accelerate particles, but generally of lower energy than the particles accelerated by CME-driven shocks. Thus both closed and open field structures on the Sun can seriously alter the conditions in the near-Earth space environment. While we understand the overall effect of the energetic phenomena on the heliosphere, we still do not understand how these are initiated at the Sun. Future observations from space missions such as STEREO, Hinode and the Solar Dynamics Observatory are expected to provide crucial data in order to make progress in understanding the initiation of energetic phenomena.

ACKNOWLEDGMENTS

I thank S. Yashiro and P. Makela for help with some figures and J. Schmidt for a careful reading of the manuscript. This work was supported by NASA's SR&T and LWS TR&T programs.

REFERENCES

1. G. E. Hale & S. B. Nicholson, *Astrophys. J.* **62**, 270 (1925).
2. G. E. Hale, F. Ellerman, S. B. Nicholson, A. H. Joy, *Astrophys. J.* **49**, 153 (1919).
3. P. Hoyng, in *NATO ASIC Proc. 373: The Sun: A Laboratory for Astrophysics*, edited by J. T. Schmelz and J. C. Brown, 99–138 (1992).
4. P. K. Manoharan, *this volume* (2007).
5. N. Gopalswamy, K. Shibasaki, B. J. Thompson, J. Gurman, C. DeForest, *J. Geophys. Res.* **104**, 9767–9780 (1999).
6. D. M. Hassler, I. E. Dammasch, P. Lemaire, P. Brekke, W. Curdt, H. E. Mason, J.-C. Vial, K. Wilhelm, *Science* **283**, 810 (1999).
7. C.-Y. Tu, C. Zhou, E. Marsch, L.-D. Xia, L. Zhao, J.-X. Wang, K. Wilhelm, *Science* **308**, 519–523 (2005).
8. J. B. Zirker, *Rev. Geophys. Space Phys.* **15**, 257–269 (1977).
9. Z. Svestka, *Solar Flares* Springer-Verlag Berlin Heidelberg, (1976).
10. H. Zirin, *Astrophysics of the Sun*, Cambridge and New York, Cambridge University Press, (1988).
11. B. R.Dennis, *Solar Phys.* **100**, 465–490 (1985).
12. J. Lee, D. E. Gary&K. Shibasaki, *Astrophys. J.* **531**, 1109–1120 (2000).
13. L. Fletcher & H. Hudson, *Solar Phys.* **204**, 69–89 (2001).
14. G. H. Share & R. J. Murphy, in *Solar Eruptions and Energetic Particles*, edited by N. Gopalswamy, R. Mewaldt, & J. Torsti, Geophysical Monograph 165, 177–188 (2006).
15. M. R. Kundu, *Solar Radio Astronomy* New York: Interscience Publication, 1965.
16. V. V.Zheleznyakov, *Radio Emission of the Sun and Planets*, La Recherche Spatiale, 1970.
17. R. Tousey, *Space Res.* **13**, 713 (1973).
18. E. Tandberg-Hanssen, *The Nature of Solar Prominences*, Astrophysics and Space Science Library, vol. 199, Dordrecht: Kluwer Academic Publishers, 1995.
19. R. Payne-Scott, D. E. Yabsley & J. G. Bolton, *Nature* **160**, 256 (1947).
20. A. C. Riddle, *Solar Phys.* **13**, 448 (1970).
21. A. Boischot, *Comptes Rendus Acad. Sci.* **244**, 1326 (1957).
22. R. T. Hansen, C. J. Garcia, R. J.-M. Grognard, K. V. Sheridan, *Proc. ASA* **2**, 57 (1978).
23. H. L. DeMastus, W. J. Wagner, R. D. Robinson, *Solar Phys.* **31**, 449 (1973).
24. J. Hirshberg, S. J. Bame, D. E. Robbins, *Solar Phys.* **23**, 467 (1972).

25. N. Gopalswamy, in *ASSL Vol. 317: The Sun and the Heliosphere as an Integrated System*, edited by G. Poletto & S. T. Suess, Kluwer, Boston, 201 (2004).
26. H. Kunow, N. U. Crooker, J. A. Linker, R. Schwenn, R. von Steiger, *Coronal Mass Ejections*, Kluwer, Boston, 2007.
27. N. Gopalswamy, R. Mewaldt, J. Torsti, *Solar Eruptions and Energetic Particles*, Geophysical Union Geophysical Monograph Series 165, 2006.
28. G. E. Brueckner and 14 colleagues, *Solar Phys.* **162**, 357–402 (1995).
29. J. Chen, R. A. Howard, G. E. Brueckner, R. Santoro, J. Krall, S. E. Paswaters, O. C. St. Cyr, R. Schwenn, P. Lamy, G. M. Simnett, *Astrophys. J.* **490**, L191 (1997).
30. N. R. Sheeley, J. H. Walters, Y.-M. Wang, R. A. Howard, *J. Geophys. Res.* **104**, 24739–24768 (1999).
31. R. A. Howard, D. J. Michels, N. R. Sheeley Jr, M. J. Koomen, *Astrophys. J.* **263**, L101–L104 (1982).
32. A. J. Hundhausen, in *Coronal Mass Ejections*, AGU Geophysical Monograph 99, edited by N. Crooker, J.A. Joselyn, & J. Feynman, 1 (1997).
33. S. Yashiro, N. Gopalswamy, G. Michalek, O. C. St. Cyr, S. P. Plunkett, N. B. Rich, R. A. Howard, *J. Geophys. Res.* **109**, 7105 (2004).
34. B. E. Wood, M. Karovska, J. W. Cook, R. A. Howard, G. E. Brueckner, *Astrophys. J.* **523**, 444–449 (1999).
35. N. Gopalswamy, S. Yashiro, M. L. Kaiser, R. A. Howard, J.-L. Bougeret, *J. Geophys. Res.* **106**, 29219–29230 (2001).
36. N. Gopalswamy, S. Yashiro, Y. Liu, G. Michalek, A. Vourlidas, M. L., Kaiser, R. A. Howard, *J. Geophys. Res.* **110**, 9 (2005).
37. A. J.Hundhausen, *J. Geophys. Res.* **98**, 13177 (1993).
38. N. Gopalswamy, A. Lara, S. Yashiro, S. Nunes, R. A. Howard, in *Coronal mass ejection activity during solar cycle 23, ESA SP-535: Solar Variability as an Input to the Earth's Environment*, 403–414 (2003).
39. N. Gopalswamy, A. Lara, S. Yashiro, R. A. Howard, *Astrophys. J.* **598**, L63–L66 (2003).
40. D. F. Webb & R. A. Howard, *J. Geophys. Res.* **99**, 4201–4220 (1994).
41. A. Hundhausen, in *The Many Faces of the Sun: a Summary of the Results from NASA's Solar Maximum Mission*, edited by K. T. Strong, J. L. R. Saba, B. M. Haisch, & J. T. Schmelz (New York: Springer), 143 (1999).
42. N. Gopalswamy, S. Yashiro & S. Akiyama, in *Solar Influence on the Heliosphere and Earth's Environment: Recent Progress and Prospects*, edited by N. Gopalswamy & A. Bhattacharyya, Quest Publications, Mumbai, 79–84 (2006).
43. W. J. Wagner, *Ann. Rev. Astron. Astrophys.* **22**, 267–289 (1984).
44. G. Newkirk Jr., A. J. Hundhausen, V. Pizzo, *J. Geophys. Res.* **86**, 5387–5396 (1981).
45. A. Lara, N. Gopalswamy, R. A. Caballero-López, S. Yashiro, H. Xie, J. F. Valdés-Galicia, *Astrophys. J.* **625**, 441–450 (2005).
46. N. Gopalswamy, N. Nitta, P. K. Manoharan, A. Raoult, M. Pick, *Astron. Astrophys.* **347**, 684–695 (1999).
47. B. J. Thompson, J. B. Gurman, W. M. Neupert, J. S. Newmark, J.-P. Delaboudinière, O. C. St. Cyr, S.Stezelberger, K. P., Dere, R. A. Howard, D. J. Michels, *Astrophys. J.* **517**, L151–L154 (1999).
48. N. Gopalswamy, M. L. Kaiser, R. J. MacDowall, M. J. Reiner, B. J. Thompson, O. C. St. Cyr, in *American Institute of Physics Conference Series 471*, 641 (1999).
49. B. J. Thompson, E. W. Cliver, N. Nitta, C. Delannée, J.-P. Delaboudinière, *Geophys. Res. Lett.* **27**, 1431–1434 (2000).
50. N. Gopalswamy, M. R. Kundu, Y. Hanaoka, S. Enome, J. R. Lemen, M. Akioka, *New Astron.* **1**, 207–213 (1996).
51. A. H. McAllister, M. Dryer, P. McIntosh, H. Singer, L. Weiss, *J. Geophys. Res.* **101**, 13497–13516 (1996).
52. N. Gopalswamy, *Adv. Space Res.* **31**, 869–881 (2003).
53. D. Tripathi, V. Bothmer, H. Cremades, *Astron. Astrophys.* **422**, 337–349 (2004).
54. A. Klassen, H. Aurass, G. Mann, B. J. Thompson, *Astron. Astrophys. Sup.* **141**, 357–369 (2000).
55. N. Gopalswamy, *Radio Astronomy at Long Wavelengths, AGU Monograph 119*, edited by R. G. Stone, K. W. Weiler, M. L. Goldstein, & J.-L. Bougeret, 123 (2000).
56. Y. Hanaoka, and 19 colleagues, *PASJ* **46**, 205–216 (1994).

57. N. Gopalswamy, M. Shimojo, W. Lu, S. Yashiro, K. Shibasaki, R. A. Howard, *Astrophys. J.* **586**, 562–578 (2003).
58. N. Gopalswamy, in *NRO Report No. 479*, edited by T. S. Bastian, N. Gopalswamy & K. Shibasaki, 141–152 (1999).
59. K. V. Sheridan, B. V. Jackson, D. J. McLean, G. A. Dulk, *Proc. ASA* **3**, 249–250 (1978).
60. N. Gopalswamy & M. R. Kundu, *Astrophys. J.* **390**, L37–L39 (19 92).
61. R. Ramesh & C. V. Sastry, *Astron. Astrophys.* **358**, 749–752 (20 00).
62. C. Kathiravan, & R. Ramesh, *Astrophys. J.* **610**, 532–536 (2 004).
63. D. Maia, M. Pick, A. Vourlidas, R. Howard, *Astrophys. J.* **528**, L49–L5 1 (2000).
64. E. J. Schmahl, *Aust. J. Phys. Astrophy. Suppl.* **29**, 1 (1973).
65. N. Gopalswamy & M. R. Kundu, *Solar Phys.* **122**, 145–173 (19 89).
66. N. Gopalswamy, *Planetary and Space Science* **52**, 1399–1413 (2004).
67. N. Gopalswamy, E. Aguilar-Rodriguez, S. Yashiro, S. Nunes, M. L. Kaiser, R. A. Howard, *J. Geophys. Res.* **110**, 12 (2005).
68. L. Burlaga, E. Sittler, F. Mariani, R. Schwenn, *J. Geophys. Res.* **86**, 6673–6684 (1981).
69. S. W. Kahler, *Ann. Rev. Astron. Astrophys.* **30**, 113–141 (1992).
70. R. A. Harrison, *Adv. Space Res.* **11**, 25–36 (1991).
71. Y.-J. Moon, G. S. Choe, H. Wang, Y. D Park, N. Gopalswamy, G. Yang, S. Yashiro, *Astrophys. J.* **581**, 694–702 (2002).
72. S. Yashiro, N. Gopalswamy, S. Akiyama, G. Michalek, R. A. Howard, *J. Geophys. Res.* **110**, 12 (2005).
73. S. Yashiro, S. Akiyama, N. Gopalswamy, R. A. Howard, *Astrophys. J.* **650**, L143–L146 (2006).
74. H. S. Hudson, *Solar Phys.* **133**, 357–369 (1991).
75. H. R. M. Kay, J. L. Culhane, L. K. Harra, S. A. Matthews, *Adv. Space Res.* **32**, 1051–1056 (2003).
76. R. H. Munro, J. T. Gosling, E. Hildner, R. M. MacQueen, A. I. Poland, C. L. Ross, *Solar Phys.* **61**, 201–215 (1979).
77. J. Lin, T. G. Forbes, P. A. Isenberg, P. Demoulin, *Astrophys. J.* **504**, 1006 (1998).
78. T. Amari, J. F. Luciani, Z. Mikic, J. Linker, *Astrophys. J.* **529**, L49–L52 (2000).
79. J. A. Linker, Z. Mikić, R. Lionello, P. Riley, T. Amari, D. Odstrcil, *Physics of Plasmas* **10**, 1971–1978 (2000).
80. S. K. Antiochos, C. R. DeVore, J. A. Klimchuk, *Astrophys. J.* **510**, 485–493 (1999).
81. J. Chen, *J. Geophys. Res.* **101**, 27499–27520 (1996).
82. R. L. Moore & A. C. Sterling, *Solar Eruptions and Energetic Particles*, edited by N. Gopalswamy, R. Mewaldt, & J. Torsti, Geophysical Monograph 165, 43–57 (2006).
83. T. G. Forbes, and 13 colleagues, *Space Sci. Rev.* **123**, 251–302 (2006).
84. N. Gopalswamy, A. Lara, S. Yashiro, M. L. Kaiser, R. A. Howard, *J. Geophys. Res.* **106**, 29207–29218 (2001).
85. P. Riley, J. A. Linker, Z. Mikić, D. Odstrcil, T. H. Zurbuchen, D. Lario, R. P. Lepping, *J. Geophys. Res.* **108**, 2–1 (2003).
86. S. E. Forbush, *Phys. Rev.* **70**, 771–772 (1946).
87. R. P. Lin, *Solar Phys.* **113**, 217 (1987).
88. D. V. Reames, *Space Sci. Rev.* **90**, 413–491 (1999).
89. E. W. Cliver, in *American Institute of Physics Conference Series* **374**, 45 (1996).
90. J. Torsti, J. Laivola, L. Kocharov, *Astron. Astrophys.* **408**, L1–L4 (2003).
91. M. J. Reiner, *ESA SP-535: Solar Variability as an Input to the Earth's Environment*, 841–851 2003).
92. A. J. Tylka & M. A. Lee, *Solar Eruptions and Energetic Particles*, edited by N. Gopalswamy, R. Mewaldt, & J. Torsti, Geophysical Monograph 165, 263–274 (2006).
93. E. W. Cliver & A. G. Ling, *Astrophys. J.* **658**, 1349–1356 (2007).
94. G. M. Mason, J. E. Mazur, J. R. Dwyer, *Astrophys. J.* **525**, L133–L136 (1999).
95. S. W. Kahler, *J. Geophys. Res.* **106**, 20947–20956 (2001).
96. N. Gopalswamy, S. Yashiro, A. Lara, M. L. Kaiser, B. J. Thompson, P. T. Gallagher, R. A. Howard, *Geophys. Res. Lett.* **30**, 3–1 (2003).
97. N. Gopalswamy, S. Yashiro, S. Krucker, G. Stenborg, R. A. Howard, *J. Geophys. Res.* **109**, 12105 (2004).
98. N. Gopalswamy, S. Yashiro, G. Michałek, M. L. Kaiser, R. A. Howard, D. V. Reames, R. Leske, T. von Rosenvinge, *Astrophys. J.* **572**, L103–L107 (2002).

99. J. Schmidt & P. Cargill, *Ann. Geophysicae* **22**, 2245–2254 (2004).
100. S. Yashiro, N. Gopalswamy, E. W. Cliver, D. V. Reames, M. L. Kaiser, R. A. Howard, in *The Solar-B Mission and the Forefront of Solar Physics ASP Conference Series 325*, 401 (2004).
101. S. W. Kahler, D. V. Reames, N. R. Sheeley, Jr., *Astrophys. J.* **562**, 558–565 (2001).
102. N. Gopalswamy, S. Yashiro, M. L. Kaiser, R. A. Howard, *Adv. Space Res.* **32**, 2613–2618 (2003).
103. A. J. Tylka, P. R. Boberg, C. M. S. Cohen, W. F. Dietrich, C. G Maclennan, G. M. Mason, C. K. Ng, D. V. Reames, *Astrophys. J.* **581**, L119–L123 (2002).
104. N. Gopalswamy, S. Yashiro, & S. Akiyama, *J. Geophys. Res.* in press (2007).
105. G. M. Lindsay, J. G. Luhmann, C. T. Russell, J. T. Gosling, *J. Geophys. Res.* **104**, 12515–12524 (1999).
106. N. Gopalswamy, A. Lara, P. K. Manoharan, R. A. Howard, *Adv. Space Res.* **36(12)**, 2289–2294 (2005).
107. H. Xie, N. Gopalswamy, L. Ofman, O. C. St. Cyr, G. Michalek, A. Lara, S. Yashiro, *Space Weather* **4**, 10002 (2006).
108. R. Schwenn, A. dal Lago, E. Huttunen, W. D. Gonzalez, *Ann. Geophysicae* **23**, 1033–1059 (2005).